

Simulating Hadronic Physics on NISQ devices using Basis Light-Front Quantization

Michael Kreshchuk,¹ Shaoyang Jia,^{2,3} William M. Kirby,¹
Gary Goldstein,¹ James P. Vary,² and Peter J. Love^{1,4}

¹*Department of Physics and Astronomy, Tufts University, Medford, MA 02155, USA*

²*Department of Physics and Astronomy, Iowa State University, Ames, IA 50011, USA*

³*Physics Division, Argonne National Laboratory, Argonne, IL 60439, USA*

⁴*Computational Science Initiative, Brookhaven National Laboratory, Upton, NY 11973, USA*

The analogy between quantum chemistry and light-front quantum field theory, first noted by Kenneth G. Wilson, serves as motivation to develop light-front quantum simulation of quantum field theory. We demonstrate how calculations of hadron structure can be performed on Noisy Intermediate-Scale Quantum devices within the Basis Light-Front Quantization framework. We calculate the light-front wave functions of pions using an effective light-front Hamiltonian in a basis representation on a current quantum processor. We use the Variational Quantum Eigensolver to find the ground state energy and wave function, which is subsequently used to calculate pion mass radius, decay constant, elastic form factor, and charge radius.

CONTENTS

I. Introduction	1	2. The BLFQ-NJL Hamiltonian in the $J_z = 0$ block	16
II. Basis Light-Front Quantization	3	B. Analytical expressions for integrals of basis functions	17
A. Overview	3	1. Integrals for the calculation of the decay constant	17
B. The effective Hamiltonian of the BLFQ-NJL model	3	2. Integrals for the mass radius	17
C. The basis function representations of wave functions for valence quarks of mesons	4	3. Longitudinal integrals	18
III. Computing observables from the valence LFWF	5	C. The electromagnetic form factors in the basis representation	19
A. The decay constant	5	1. Reduction of the formula for the electromagnetic form factors in the valence Fock sector of mesons	19
B. The mass radius	6	2. The electromagnetic form factors in the basis representation	20
C. Parton distribution function of valence quarks	7	D. Multi-qubit observables for the $J_z = 0$ sector of the $N_{\max} = L_{\max} = 0$, $M_{\max} = 2$ Hamiltonian	22
D. The elastic form factor for pseudoscalar mesons	7	E. Bravyi-Kitaev encoding	22
IV. Quantum-Computational Methods	8	References	23
A. Direct encoding	9		
Efficiency analysis	10		
B. Compact encoding	11		
Efficiency analysis	11		
V. Results	12		
VI. Discussion	14		
Acknowledgments	15		
A. Hamiltonian in the basis representation	16		
1. Unitary transformation to the fixed J_z blocks	16		

I. INTRODUCTION

Quantum simulation of quantum field theory (QFT) is a promising application of quantum computing that has recently seen a surge in interest [1–32]. In our previous work [33] we demonstrated that the light-front (LF) quantization of quantum field theory provides a natural framework for *ab initio*

digital quantum simulation. The Discretized Light-Cone Quantization (DLCQ) technique allows one to significantly reduce the quantum-computational resources when compared to lattice approaches.

In the present paper, we continue our program of investigating quantum simulation in the light-front (LF) formulation, and develop an approach to simulating field theory based on the Basis Light-Front Quantization (BLFQ) [34, 35] technique. The basis-function expansion allows us to further reduce the need for computational resources, making calculations accessible for existing quantum devices.

In [33] we developed quantum algorithms based on simulating time evolution and adiabatic state preparation. In this work, we instead aim for near-term devices by adopting the Variational Quantum Eigensolver (VQE) paradigm: this allows us to implement a demonstration on the IBM Vigo quantum processor. VQE is a hybrid quantum-classical algorithm. The classical computer optimizes the expectation value of the Hamiltonian, which is repeatedly evaluated on a quantum computer. The classical computer/algorithm optimizes the parameters of this ansatz to minimize the ground state energy.

The resulting parametrized quantum circuit approximately prepares the ground state wave function of the Hamiltonian. Thus once the VQE procedure is complete, we can compute the expectation values of other observables in this approximate ground state.

The DLCQ and BLFQ paradigms provide alternative approaches to describing relativistic interactions. While both are, in principle, *ab initio* frameworks, DLCQ studies the system starting from the light-front Hamiltonian quantized in the traditional free-field basis placed on a discrete momentum grid. BLFQ starts from the same light-front Hamiltonian but quantizes it in terms of modes tailored to the symmetries of the system under consideration in order to construct an computationally efficient representation of the Hamiltonian. Since each represents a choice of basis spaces for the fields, they should yield the same results in fully converged calculations, *i.e.*, in their respective continuum limits.

Having much in common with *ab initio* quantum chemistry and nuclear theory, the BLFQ formulation provides an ideal framework for benchmarking NISQ devices and testing existing algorithms on physically relevant problems such as the calculation of hadronic spectra [36–39] and parton distribution functions (PDFs) [40–42]. In essence, BLFQ amounts to (1) Choosing the effective field theory most efficiently describing the problem of interest, (2) Quantizing the system in the light-cone coordinates, (3) Non-perturbatively solving the theory in the most suit-

able basis. This results in an efficient representation of the QFT problem under study. One typically starts with a fixed-particle-number formulation, effectively reducing the QFT setting to a relativistic quantum-mechanical many-body problem. In many cases, already at this level one can obtain results with suitable precision to make meaningful comparisons with experimental results [37–43].

In this article, we consider the dynamics of valence quarks for light mesons on the light front using the Hamiltonian from [43]. This Hamiltonian includes the kinetic energy, the confinement potential in both the longitudinal and the transverse directions [37], and the Nambu–Jona-Lasinio interaction [44] to account for the chiral interactions among quarks. We limit ourselves to the valence Fock sector of mesons while working with relative momentum variables. The dependence of the light-front wave functions for these valence quarks on the relative momentum is expanded in terms of orthonormal basis functions. After implementing finite cut-offs in this expansion, the light-front Hamiltonian becomes a hermitian matrix in the basis representation. We use the same scheme as in Ref. [43] to fix our model parameters at each choice of basis cut-offs. We illustrate our ideas by choosing an effective Hamiltonian for the light meson system, and running the VQE minimization on the IBM Vigo machine to calculate the squared pion mass. Using the resulting wave function, we calculate squared mass, decay constant, mass radius, electromagnetic form factor, and charge radius of the pion.

The two different ansätze we consider in this paper are based on different ways of encoding physical states on the quantum computer. Within the *direct encoding* one stores the occupancies of the second-quantized states in the unary form and uses the Unitary Coupled Cluster ansatz for state preparation. Within a more efficient *compact encoding*, one stores the occupancies in the binary form, which requires logarithmically fewer qubits and allows one to prepare an ansatz state using the arbitrary state preparation algorithms, given that the particle number is fixed and small.

In Sec. II, we provide a summary of the BLFQ formalism and a representation of basis functions, which we used throughout the paper. In Sec. III, we derive expressions for various observables in the chosen basis. In Sec. IV we describe two variations of the VQE algorithm, and show the results of running it on an existing quantum computer.

II. BASIS LIGHT-FRONT QUANTIZATION

A. Overview

The light-front quantization approach specifies the commutation relation of fields at equal light-front time [45]. In contrast to the Lagrangian formulation of equal-time quantization, the field theory dynamics after light-front quantization is governed by a light-front Hamiltonian [45] responsible for the light-front time evolution of the system. Quantizing a QFT on the light front has a number of advantages: triviality of the vacuum, absence of ghost fields in the light-cone gauge, Hamiltonian sparsity, and the simple form of observables in terms of the wave functions. Within the light-front approach, the bound state masses and associated wave functions are solvable from the light-front-time-independent Schrödinger equation.

In [33] we developed a simulation algorithm based on the DLCQ, allowing one to reduce the resource requirements for the *ab initio* simulation of QFT by a few orders of magnitude. In this work, we further reduce the computational requirements into the range of the capabilities of existing quantum devices. We achieve this by employing the framework of BLFQ [34, 35].

Within BLFQ, a field is expanded in terms of second-quantized Fock states representing occupancies of modes (first-quantized basis functions), and there is no *a priori* limit on the degrees of freedom [34, 46]. Accordingly, our algorithms are designed to efficiently simulate QFT applications where particle number is not conserved. However, for QFTs at low resolution, BLFQ is often restricted to the valence degrees of freedom, allowing the adoption of this restriction in order to implement quantum simulations on an existing quantum chip. These experiments represent the first stage shown in Fig. I, which illustrates a progression of methods that scale towards fault-tolerant simulation of QFTs in the quantum supremacy regime. However, the methods we propose apply to the first three stages in Tab. I. The final stage was discussed in [33].

Previous development of BLFQ for the heavy mesons is partially based on the holographic confinement potential between the valence quark and antiquark in the holographic transverse directions [37–39]. This potential is supplemented by a longitudinal confinement potential to attain a 3-dimensional spherical confinement potential in the nonrelativistic limit. These potentials are constructed independent of the spins for the quark and the antiquark and they are governed by a single overall strength parameter.

In addition to the kinetic energy and the confinement potentials, they form the baseline Hamiltonian that is analytically solvable and defines our basis functions [37, 43]. These basis functions possess desired spatial symmetries and boost invariances. The derived effective one-gluon exchange interaction based on the gauge dynamics serves as the spin-orbit interaction and incorporates a running coupling [37].

In this article we adopt the Hamiltonian in Ref. [43] for the light mesons. Specifically the same confinement potential forms as those in Ref. [37] are implemented. However, we do not include the one-gluon exchange because the interactions for light quarks manifest from the chiral symmetry, which is insufficiently accounted for by a perturbative expansion of the gauge interaction. Instead, we resort to the Nambu–Jona-Lasinio (NJL) model for the chiral interaction of these quarks [44, 47, 48]. Within our basis representation, the matrix elements of the NJL interaction can be calculated analytically [43]. We compute the lowest mass eigenvalue and its corresponding eigenvector, its light-front wave function, using the algorithm to be described in Section IV. We then calculate observables based on this eigenvector.

B. The effective Hamiltonian of the BLFQ-NJL model

The light-front wave functions (LFWFs) of the valence quarks for the π^+ meson and the K^+ meson have been solved from Ref. [43] in the basis light-front quantization (BLFQ) framework using Nambu–Jona-Lasinio interactions [44, 47–49] on a classical computer. Specifically, one first truncates the light-front wave-function for the mesons to the valence quark Fock sector such that the state vector is expressed as

$$\begin{aligned}
 |\Psi(P^+, \vec{P}^\perp)\rangle &= \sum_{r,s} \int_0^1 \frac{dx}{4\pi x(1-x)} \\
 &\times \int \frac{d\vec{\kappa}^\perp}{(2\pi)^2} \psi_{rs}(x, \vec{\kappa}^\perp) \times b_r^\dagger(xP^+, \vec{\kappa}^\perp + x\vec{P}^\perp) \\
 &\times d_s^\dagger((1-x)P^+, -\vec{\kappa}^\perp + (1-x)\vec{P}^\perp) |0\rangle.
 \end{aligned} \tag{1}$$

where $P = k+p$ is the total momentum of the meson, $x = k^+/P^+$ is the longitudinal momentum fraction carried by the valence quark, and $\vec{\kappa}^\perp = \vec{k}^\perp - x\vec{P}^\perp$ is the relative transverse momentum.

In order to solve for the LFWFs for the valence quarks inside light mesons, we adopt the effective Hamiltonian that can be represented as a basis-

Regime	VQE			Fault-tolerant
	Two-body sector BLFQ, relative coordinate basis	Valence sector BLFQ, single- coordinate basis	Multi-particle BLFQ, single- coordinate basis	Multi-particle DLCQ, single- coordinate basis
Encoding	Compact	Compact / Direct		Compact
State preparation	Arbitrary state preparation	Arbitrary state preparation / Unitary Coupled Cluster / QITE		Adiabatic state preparation
Measurement	Pauli	Pauli / Sparse		Sparse

Table I. Flow of growing complexity and computational resources (left to right) for quantum simulation of quantum field theory on the light-front. Basis light-front quantization (BLFQ) may be considered to encapsulate discrete light-cone quantization (DLCQ). However, we use the distinct terms here to emphasize that classical preprocessing is used in BLFQ with minimal bases for the purpose of obtaining approximations using relatively few quantum resources. The goal is to accelerate convergence to the continuum limit for bound state observables and, hence, to optimally use existing quantum resources in the NISQ era for these problems. Treatment of open systems, such as resonances and strong decays, will likely require DLCQ to be implemented on future fault-tolerant quantum computers.

diagonal term and the NJL interaction:

$$H_{\text{eff}} = H_0 + H_{\text{int}}^{\text{eff}}. \quad (2)$$

The basis-diagonal term H_0 contains the kinetic energy of the valence quarks, the transverse confinement potential, and the longitudinal confinement potential. In the valence Fock sector of mesons, this term takes the form of

$$H_0 = \frac{(\vec{\kappa}_\perp)^2 + \mathbf{m}^2}{x} + \frac{(\vec{\kappa}_\perp)^2 + \bar{\mathbf{m}}^2}{1-x} + b^4 x(1-x) \vec{r}_\perp^2 - \frac{b^4}{(\mathbf{m} + \bar{\mathbf{m}})^2} \partial_x x(1-x) \partial_x, \quad (3)$$

where x is the longitudinal momentum fraction carried by the valence quark and $\vec{\kappa}_\perp$ is the relative transverse momentum of the valence quarks. The masses of the valence quark and the valence antiquark are given by \mathbf{m} and $\bar{\mathbf{m}}$, respectively. In addition, b specifies the strength of the confinement potentials. This part of the Hamiltonian has analytic solutions that constitute the basis states for the BLFQ approach as will be seen in detail in Subsection II C.

When quarks in the confinement region are the retained degrees of freedom, the strong interaction among them can be understood to arise from the global chiral symmetry, an approximate symmetry of quantum chromodynamics. To model this chiral interaction, we employ the interaction in the scalar-pseudoscalar channel of the color-singlet NJL model [44]. Specifically, we ignore both the instantaneous interaction and the self-energy correction from the NJL interaction to obtain the following term in

the total Hamiltonian:

$$H_{\text{int}}^{\text{eff}} = H_{\text{NJL},\pi}^{\text{eff}} = \int dx^- \int d\vec{x}_\perp \left(-\frac{G_\pi P^+}{2} \times \left[(\bar{\psi}\psi)^2 + (\bar{\psi}i\gamma_5\vec{\tau}\psi)^2 \right] \right), \quad (4)$$

Here ψ is the fermion field operator, G_π is the NJL coupling constant, and P^+ is the total light-front longitudinal momentum of the system. We then expand eq. (4) into relevant combinations of ladder operators for the quark fields. In the basis representation, this term further takes the form of a hermitian matrix, the elements of which can be calculated analytically [43].

In this work, we solve the eigenvalue problem defined by eq. (2) in the total angular momentum $J_z = 0$ block with the lowest eigenstates of H_0 forming the longitudinal and radial basis states for the interacting Hamiltonian. In this representation, the effective Hamiltonian takes the form of a 4-by-4 matrix indexed by the basis quantum number θ that specifies the angular and spin excitations. The explicit expressions for elements in this matrix are given in Appendix A 2.

C. The basis function representations of wave functions for valence quarks of mesons

We adopt the following expansion of the light-front wave function for the valence quarks given by eq. (1):

$$\psi_{rs}(x, \vec{\kappa}_\perp) = \sum_{nml} \psi_{nmlrs} \phi_{nm} \left(\frac{\vec{\kappa}_\perp}{\sqrt{x(1-x)}}; b \right) \chi_l(x), \quad (5)$$

where $\psi_{nm\ell r s}$ is the expansion coefficient, ϕ_{nm} is a 2-dimensional (2D) harmonic oscillator (HO) eigenfunction, and χ_l is the longitudinal basis function. Here r and s are the spin indices of the quark and the anti-quark. Each term in eq. (5) is an eigenfunction of H_0 in eq. (3). Explicitly, ϕ_{nm} is defined as

$$\begin{aligned} \phi_{nm}(\vec{q}^\perp; b) &= \frac{1}{b} \sqrt{\frac{4\pi n!}{(n+|m|)!}} \left(\frac{|\vec{q}^\perp|}{b}\right)^{|m|} \\ &\times \exp\left(-\frac{\vec{q}^{\perp 2}}{2b^2}\right) \times L_n^{|m|}\left(\frac{\vec{q}^{\perp 2}}{b^2}\right) \exp^{im\varphi}, \end{aligned} \quad (6)$$

with $\tan(\varphi) = q^2/q^1$ and $L_n^{|m|}$ being the associated Laguerre function. The parameter b sets the scale of the harmonic oscillator eigenfunction, which we choose to be identical to the confining strength in the light-front Hamiltonian. Meanwhile, $\chi_l(x)$ is given by

$$\begin{aligned} \chi_l(x; \alpha, \beta) &= \sqrt{4\pi(2l + \alpha + \beta + 1)} \\ &\times \sqrt{\frac{\Gamma(l+1)\Gamma(l + \alpha + \beta + 1)}{\Gamma(l + \alpha + 1)\Gamma(l + \beta + 1)}} \\ &\times x^{\beta/2}(1-x)^{\alpha/2} P_l^{(\alpha, \beta)}(2x-1), \end{aligned} \quad (7)$$

with $P_l^{(\alpha, \beta)}(z)$ being the Jacobi polynomial and

$$\alpha = 2\bar{\mathbf{m}}(\mathbf{m} + \bar{\mathbf{m}})/\kappa^2, \quad (8a)$$

$$\beta = 2\mathbf{m}(\mathbf{m} + \bar{\mathbf{m}})/\kappa^2. \quad (8b)$$

When we solve the eigenvalue problem defined by the BLFQ-NJL Hamiltonian, the following cutoffs on the basis quantum numbers following Ref. [43] are imposed:

$$\begin{cases} 0 \leq n \leq N_{\max} \\ -M_{\max} \leq m \leq M_{\max} \\ 0 \leq l \leq L_{\max} \end{cases}. \quad (9)$$

Because truncations on different basis quantum numbers are independent, we call this truncation scheme the orthogonal enumeration. Such a scheme allows us to solve simultaneously for eigenstates with different azimuthal angular momentum projection J_z since it is a good quantum number in this basis. The size of the Hamiltonian in the basis representation with this orthogonal enumeration is n_{H} -by- n_{H} , with

$$n_{\text{H}} = 4(N_{\max} + 1)(2M_{\max} + 1)(L_{\max} + 1). \quad (10)$$

However, the capacity of NISQ devices motivates further reduction in the dimension of the Hilbert

space spanned by our basis representation. Specifically, because eigenfunctions of this Hamiltonian have fixed azimuthal angular momentum projection J_z , the basis quantum number θ indexes specific combinations of the spin and orbital bases in the orthogonal enumeration as specified in Appendix A 1. Each basis state in the fixed J_z block is then given by the basis quantum numbers n , l , and θ . In the limit of $M_{\max} = 2$, the unitary transformation that relates the bases in the fixed J_z blocks to those in the orthogonal enumeration is given by Table V. The degeneracy in the basis quantum number θ in each J_z block is apparent in Table V. For example when $J_z = 0$, this degeneracy is $d_\theta = 4$. With a given set of (n, l, θ) in a given J_z block, we take the convention such that the index of this basis is given by

$$a(n, l, \theta) = [n(L_{\max} + 1) + l]d_\theta + \theta. \quad (11)$$

For a given index, the corresponding basis quantum numbers can be easily calculated. Consequently, the size of the Hamiltonian for a fixed J_z in this new enumeration becomes

$$n_{\text{H}0} = d_\theta(N_{\max} + 1)(L_{\max} + 1), \quad (12)$$

which is smaller than n_{H} given by eq. (10). This provides an example of how one may exploit the symmetries embedded in the chosen BLFQ to achieve gains in computational efficiency.

III. COMPUTING OBSERVABLES FROM THE VALENCE LFWF

One of the many advantages of the light-front approach to quantum field theories is that observables for bound states can be easily extracted from light-front wave functions. Explicitly, measurement operators corresponding to physical observables usually take a simple form, resulting in efficient measurements on a quantum computer (see Sec. IV and App. D). In this section, we demonstrate how to calculate the decay constant, mass radius, valence parton distribution function, and elastic form factor.

A. The decay constant

The meson decay constants are defined as the matrix elements of current operators between the vacuum and the meson wavefunctions [37]. They correspond to amplitudes of the wavefunctions at the coordinate-space origin. Specifically, the decay constants for scalar mesons (f_S), pseudoscalar mesons

(f_P), vector mesons (f_V), and axial vector mesons (f_A) are defined as

$$\langle 0 | \bar{\psi} \gamma^\mu \psi | S(p) \rangle = p^\mu f_S, \quad (13a)$$

$$\langle 0 | \bar{\psi} \gamma^\mu \gamma_5 \psi | P(p) \rangle = i p^\mu f_P, \quad (13b)$$

$$\langle 0 | \bar{\psi} \gamma^\mu \psi | V(p) \rangle = \epsilon_\lambda^\mu(p) m_V f_V, \quad (13c)$$

$$\langle 0 | \bar{\psi} \gamma^\mu \gamma_5 \psi | A(p) \rangle = \epsilon_\lambda^\mu(p) m_A f_A, \quad (13d)$$

respectively. Here the polarization vector for the vector mesons is defined as

$$\epsilon_\lambda^\mu(p) = \begin{cases} \left(\frac{p^+}{m_{V,A}}, \frac{\vec{p}^{\perp 2} - m_{V,A}^2}{m_{V,A} p^+}, \frac{\vec{p}^\perp}{m_{V,A}} \right) & \text{for } \lambda = 0 \\ \left(0, \frac{2\vec{e}_\lambda^\perp \cdot \vec{p}^\perp}{p^+}, \vec{e}_\lambda^\perp \right) & \text{for } \lambda = \pm 1 \end{cases}, \quad (14)$$

with $\vec{e}_\pm^\perp = (1, \pm i)/\sqrt{2}$.

In terms of the valence-sector light-front wavefunctions, expressions for these decay constants are reduced into [37]

$$f_{P,A} = 2\sqrt{N_c} \int_0^1 \frac{dx}{4\pi\sqrt{x(1-x)}} \int \frac{d^2\kappa^\perp}{(2\pi)^2} \times \left[\psi_{+-}(x, \vec{\kappa}^\perp) - \psi_{-+}(x, \vec{\kappa}^\perp) \right] \Big|_{m_J=0}, \quad (15a)$$

$$f_{S,V} = 2\sqrt{N_c} \int_0^1 \frac{dx}{4\pi\sqrt{x(1-x)}} \int \frac{d^2\kappa^\perp}{(2\pi)^2} \times \left[\psi_{+-}(x, \vec{\kappa}^\perp) + \psi_{-+}(x, \vec{\kappa}^\perp) \right] \Big|_{m_J=0}, \quad (15b)$$

with the condition $m_J = m + s_1 + s_2 = 0$ specifying that only the states with zero angular momentum projections are used in the calculation. Here $N_c = 3$ is the number of colors.

In the basis representation, the integrals over the longitudinal momentum fraction and the relative transverse momenta in eq. (15) can be evaluated exactly. Details of this calculation can be found in Appendix B 1. Since the decay constant is linear in the wave function, we only need to calculate these integrals for each basis function. Subsequently, the decay constants in the basis representation are given by

$$f_{P,A} = 2\sqrt{\frac{N_c}{\pi}} \sum_{n,l} (-1)^n L_l(1/2, 1/2; \alpha, \beta) \times (\psi_{n0l+-} - \psi_{n0l-+}) \Big|_{m_J=0}, \quad (16)$$

$$f_{S,V} = 2\sqrt{\frac{N_c}{\pi}} \sum_{n,l} (-1)^n L_l(1/2, 1/2; \alpha, \beta) \times (\psi_{n0l+-} + \psi_{n0l-+}) \Big|_{m_J=0}, \quad (17)$$

where the longitudinal integrals $L_l(a, b; \alpha, \beta)$ are defined and given analytically in Appendix B 3. Because the overall phase of the LFWF remains undetermined by the Hamiltonian, only the absolute value of the decay constant carries physical significance. Once the LFWF $|\psi\rangle$ in our basis representation is known on a quantum computer, the calculation of the corresponding decay constant can be thought of as computing $|\langle v | \psi \rangle|$ for some fixed $|v\rangle$.

B. The mass radius

The mass radius is the square root of the expectation value for the relative transverse separation of the valence quarks. It can be calculated from the valence two-body wave-function based on eq. (33) of Ref. [37]. Specifically for the pseudoscalar mesons, we have

$$\langle r_m^2 \rangle = \frac{3}{2} \sum_{r,s} \int_0^1 \frac{dx}{4\pi} \int d\vec{r}^\perp x(1-x) \vec{r}^{\perp 2} \times \tilde{\psi}_{rs}^*(x, \vec{r}^\perp) \tilde{\psi}_{rs}(x, \vec{r}^\perp), \quad (18)$$

where $\tilde{\psi}_{rs}(x, \vec{r}^\perp)$ is the light-front wave-function depending on the longitudinal momentum fraction x and the relative transverse coordinate \vec{r}^\perp . It is related to the momentum-space wave-function by the Fourier transform in the transverse momenta $\vec{\kappa}^\perp$. Explicitly, we have

$$\tilde{\psi}_{rs}(x, \vec{r}^\perp) = \sqrt{x(1-x)} \sum_{nml} \psi_{nmlrs} \times \tilde{\phi}_{nm}(\sqrt{x(1-x)}\vec{r}^\perp) \chi_l(x), \quad (19)$$

with

$$\tilde{\phi}_{nm}(\vec{r}^\perp) = b \sqrt{\frac{n!}{(n+|m|)! \pi}} (b|\vec{r}^\perp|)^{|m|} \times \exp\left[-\frac{b^2 \vec{r}^{\perp 2}}{2}\right] L_n^{|m|}(b^2 \vec{r}^{\perp 2}) \times \exp\left[im\phi_r + i(n+|m|/2)\pi\right], \quad (20)$$

and $\tan \phi_r = r_2/r_1$.

To calculate the mass radius in terms of expansion coefficients $\psi_{nmls_1s_2}$, we first need to evaluate the fol-

lowing dimensionless integrals of the basis functions:

$$\begin{aligned}
I_m(n', m', l'; n, m, l) &\equiv \int_0^1 dx \chi_{l'}(x) \chi_l(x) \\
&\times \int_0^{+\infty} d|\vec{r}^\perp|^2 \int_0^{2\pi} \frac{d\phi_r}{8\pi} x^2 (1-x)^2 b^2 |\vec{r}^\perp|^2 \quad (21) \\
&\times \tilde{\phi}_{n', m'}^* \left(\sqrt{x(1-x)} \vec{r}^\perp \right) \tilde{\phi}_{n, m} \left(\sqrt{x(1-x)} \vec{r}^\perp \right) .
\end{aligned}$$

We then have the square of the radius given by

$$\begin{aligned}
\langle r_m^2 \rangle &= \frac{3}{2b^2} \sum_{rs} \sum_{n'm'l'nml} \psi_{n'm'l'rs}^* \\
&\times I_m(n', m', l'; n, m, l) \psi_{nmlrs} . \quad (22)
\end{aligned}$$

The explicit expression for the matrix $I_m(n', m', l'; n, m, l)$ is available in Appendix B 2, which takes the form of a hermitian operator in our basis representation.

C. Parton distribution function of valence quarks

The probability of finding a quark inside a meson carrying momentum fraction x is given by

$$\begin{aligned}
f(x) &= \frac{1}{4\pi x(1-x)} \\
&\times \sum_{rs} \int \frac{d\vec{k}^\perp}{(2\pi)^2} \psi_{rs}^*(x, \vec{k}^\perp) \psi_{rs}(x, \vec{k}^\perp) \quad (23) \\
&= \frac{1}{4\pi} \sum_{n, m, l', l, r, s} \psi_{nml'r's}^* \psi_{nmlrs} \chi_{l'}(x) \chi_l(x) ,
\end{aligned}$$

which is interpreted as the PDF for the valence quark. The PDF for the valence antiquark is given by $f(1-x)$ [40–42]. We use the solutions of ψ_{nmlrs} defined in eq. (5) to calculate the valence PDFs of mesons.

Notice that eq. (23) defines a bilinear of the light-front wave-functions in the basis representation. To compute the PDF with the LFWFs obtained from a quantum computer, let us rewrite eq. (23) as

$$f(x) = \frac{1}{4\pi} \sum_{l', l} \rho_{l', l} \chi_{l'}(x) \chi_l(x) , \quad (24a)$$

$$\rho_{l', l} = \sum_{n, m, r, s} \psi_{nml'r's}^* \psi_{nmlrs} . \quad (24b)$$

Elements of the density matrix $\rho_{l', l}$ defined in eq. (24b) can be evaluated as the expectation value of the corresponding projection operators on a quantum computer, and subsequently used to calculate the PDF in eq. (24a).

D. The elastic form factor for pseudoscalar mesons

To calculate the elastic form factors from the light-front wavefunctions within the impulse approximation where the photon interacts with the meson through the quark-photon vertex, we apply the following formula [50, 51] within the Drell-Yan frame $P'^+ = P^+$:

$$\begin{aligned}
I_{m'_J, m_J}(Q^2) &= \frac{1}{2P^+} \\
&\times \left\langle \Psi(P', m'_J) \left| \sum_f e_f \bar{\psi}_f(0) \gamma^+ \psi_f(0) \right| \Psi(P, m_J) \right\rangle \\
&= \sum_{rs} \int \frac{dx}{4\pi x(1-x)} \int \frac{d^2 k^\perp}{(2\pi)^2} \quad (25) \\
&\times \left\{ e_q \psi_{rs}^{*m'_J} \left(x, \vec{k}^\perp + (1-x)\vec{q}^\perp \right) \right. \\
&\quad \left. - e_{\bar{q}} \psi_{rs}^{*m'_J} \left(x, \vec{k}^\perp - x\vec{q}^\perp \right) \right\} \psi_{rs}^{m_J} \left(x, \vec{k}^\perp \right) ,
\end{aligned}$$

with $q = P' - P$ and $Q^2 = -q^2$. The operator inside the Dirac bracket is the charge density operator on the light front, with e_f being the charge carried by the quark of flavor f in units of the elementary charge and the summation running over all quark flavors. Additionally, e_q is the charge of the quark ($e_u = +2/3$ for an up quark). While $e_{\bar{q}}$ is the charge of the antiquark ($e_{\bar{d}} = -1/3$ for an anti-down quark). Detailed derivation of eq. (25) is given in Appendix C 1.

In the basis representation, we apply the Talmi-Moshinsky transform to simplify the integrals in the transverse momentum, leaving the longitudinal integral to be evaluated numerically for each Q^2 . Following steps in Appendix C 2, we rewrite the electromagnetic form factors into a bilinear form of the valence wave-function:

$$\begin{aligned}
I_{m'_J, m_J}(Q^2) &= \sum_{n'm'l'} \sum_{n, m, l} \sum_{r, s} \psi_{n'm'l'rs}^* \\
&\times \tilde{C}(n', m', l'; n, m, l; Q^2) \psi_{nmlrs} . \quad (26)
\end{aligned}$$

The operator \tilde{C} is defined according to eq. (C19). At a given Q^2 , the form factor can be calculated using the LFWFs obtained from a quantum computer by taking the expectation value of the Hermitian operator $C(n', m', l'; n, m, l; Q^2)$.

Specifically, the elastic form factors of the pseudoscalar mesons are given by

$$F_P(Q^2) = I_{0,0}(Q^2) . \quad (27)$$

The charge radius is then specified by the first Taylor expansion coefficient of the elastic form factor at the origin:

$$\langle r_c^2 \rangle = -6 \lim_{Q^2 \rightarrow 0} \frac{d}{dQ^2} F_P(Q^2) . \quad (28)$$

IV. QUANTUM-COMPUTATIONAL METHODS

The standard approach to quantum simulation of Hamiltonian dynamics of QFTs is as follows [52]: a) initialize the system in a certain state of the free Hamiltonian, b) adiabatically turn on the interaction, c) if necessary, evolve the system with time, and d) measure the energy (or another observable) of the system using the phase estimation algorithm [2, 7, 52]. However, near-term devices cannot perform this procedure due to limits in qubit numbers and in gate fidelities. This motivates the variational quantum eigensolver (VQE), an approach to finding Hamiltonian eigenvalues in which a NISQ device is used as a part of a hybrid quantum-classical algorithm [53]. In VQE, a quantum computer prepares a given variational state and evaluates the Hamiltonian expectation value, which a classical computer performs a gradient search to minimize (see Fig. 1). To prepare the variational state, we adopt an ansatz specified by parameters $\vec{\theta}$, which are controlled by the classical minimization.

While in [33] we focused on *ab initio* simulations which are likely to become available in the fault-tolerant regime, in this paper we investigate the use of NISQ devices for high-energy nuclear physics calculations on the light front. Therefore, unlike in [33], we formulate the problem as a VQE instance.

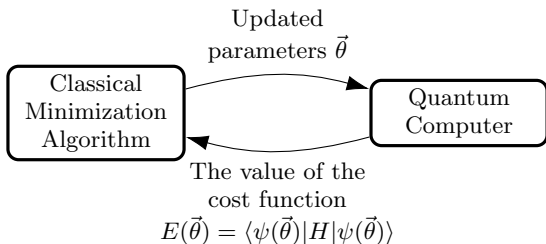


Figure 1. Schematic of the Variational Quantum Eigensolver (VQE). The parameter vector $\vec{\theta}$ completely specifies the ansatz wave function.

We begin by briefly reviewing the VQE method. For the VQE algorithm to be efficient and accurate, it is essential to come up with a parametrized ansatz

state $|\psi(\vec{\theta})\rangle$ that is easy to prepare and is expected to have significant overlap with the true ground state. Below we shall consider different choices of ansatz state preparation procedures, encodings of the physical states in a quantum computer, and classical optimization algorithms.

While using VQE for simulating a Hamiltonian problem, the major steps are:

1. Define the state/operator mapping, *i.e.*, a correspondence between the physical states and the multi-qubit states of a quantum computer, as well as the mapping between the operators acting on these spaces.
2. Choose a parametrized ansatz state. One typically writes the ansatz state as

$$|\psi(\vec{\theta})\rangle = U(\vec{\theta})|\psi_0\rangle , \quad (29)$$

where $|\psi_0\rangle$ is a fixed reference state, and $U(\vec{\theta})$ is the VQE ansatz operator. One possibility is to choose the form of $U(\vec{\theta})$ to resemble the form of the Hamiltonian evolution operator e^{iHt} [54].

3. Once the state $|\psi(\vec{\theta})\rangle$ is prepared for a given set of parameters $\vec{\theta}$, one evaluates the cost function by measuring the expectation value of the multi-qubit Hamiltonian operator:

$$E(\vec{\theta}) = \langle \psi(\vec{\theta}) | \hat{H} | \psi(\vec{\theta}) \rangle . \quad (30)$$

The algorithm can only be considered efficient if the number of measurements grows polynomially with the problem complexity (discussed further below).

4. The value of the cost function is then sent to the classical optimizer, which either determines the set of parameters for the next iteration of the algorithm, or terminates the algorithm if the desired precision has been achieved.

We shall explore two approaches to simulating problems in the BLFQ formulation, based on two different encoding schemes. The first of these is the *direct encoding*, widely used in quantum chemistry [7, 55]. In such an encoding scheme, one assigns a particular set of qubit registers to each physical (basis) degree of freedom. In application to purely fermionic systems, one may use one qubit to encode one fermionic second-quantized mode, which leads one to the Jordan-Wigner (JW) encoding [56]. Thus, one needs N qubits in order to encode N fermionic

modes. The fermionic raising and lowering operators are represented by N -local multi-qubit operators, due to the need to enforce anticommutation relations. One can alternatively employ the Bravyi-Kitaev (BK) encoding [57–60] that uses N qubits to store N fermionic modes, with operators being only $\log N$ -local. Circuits implementing VQE ansatz operators are typically based on trotterization [54].

The second encoding we employ is *compact encoding*, as was explored in [33] for front-form physics, and in the context of quantum chemistry in [7]. The idea is to only store the occupied modes of multi-particle Fock states. With this encoding, one can simulate time evolution using sparsity-based techniques, which are optimal in all parameters [17, 33, 61–64]. These methods, however, require too many gates to be used to prepare ansätze on NISQ devices. Instead, we can use arbitrary state preparation as long as we restrict to small fixed numbers of particles in the system, as discussed below.

A. Direct encoding

In order to run a simulation on a current quantum device, in this work we consider a scenario where the particle number is fixed. However, since quantum advantage is likely to be achieved only in the multi-particle regime, it is essential for our methods to be extendable to this more general scenario.

A natural way of formulating a multi-particle problem is by using the second-quantized formalism. Consider a Hamiltonian of the form

$$\hat{H} = \hat{H}_1 + \hat{H}_2 + \dots, \quad (31)$$

where

$$\hat{H}_1 = \sum_{i,j} h_{ij} a_i^\dagger a_j, \quad \hat{H}_2 = \sum_{i,j,k,l} h_{ijkl} a_i^\dagger a_j^\dagger a_k a_l. \quad (32)$$

Here h_{ij} represents the single-body interactions, while h_{ijkl} and higher-order terms correspond to many-body interactions. For the first experimental implementation, we restrict ourselves to $\hat{H} = \hat{H}_1$ (with h_{ij} being the meson valence sector BLFQ Hamiltonian matrix), for two reasons. First, owing to the efficiency of the BLFQ formulation, considering the single-body part of the Hamiltonian is oftentimes enough to give reasonably good results [36, 40, 42, 43, 65]. Second, this is suitable for benchmarking, paralleling state-of-the-art experimental results in quantum simulation of chemistry [66].

Within the JW encoding, the multi-qubit states $|\dots f_2 f_1 f_0\rangle$ mimic the second-quantized fermionic states: the qubit f_i stores the occupancy of the $(i+1)$ -th orbital (see Table II). In order to enforce anticommutation relations, the fermionic creation and annihilation operators are represented by N -local multi-qubit operators [56]. We shall use this encoding for the rest of the section; simulation in the Bravyi-Kitaev encoding is discussed in App. E.

Basis state index	Direct encoding	Compact encoding
1	$ 0001\rangle$	$ 00\rangle$
2	$ 0010\rangle$	$ 01\rangle$
3	$ 0100\rangle$	$ 10\rangle$
4	$ 1000\rangle$	$ 11\rangle$

Table II. The multi-qubit representation of the four physical one-particle states in the direct and compact encodings.

Since one typically solves the problem in a basis found by means of some classical approximation, the reference state $|\psi_0\rangle$ can be chosen to have a simple form in terms of basis vectors; in the simplest case, it may coincide with one of the basis vectors. Next, we would like to design an ansatz operator that acts on the reference state to prepare an ansatz state that ideally has large overlap with the exact ground state. An example of such an operator is the Unitary Coupled Cluster (UCC) [54]. Choosing the form of the ansatz operator to resemble the form of the Hamiltonian ensures that one can explore the regions of the Hilbert space that can be reached via the Hamiltonian time evolution, and also guarantees that the symmetries are preserved. For the Hamiltonian of the form (32) one writes the UCC as [54]

$$U(\vec{\theta}) = e^{T-T^\dagger}, \quad T = T_1 + T_2 + \dots, \quad (33)$$

$$T_1 = \sum_{\substack{i \in \text{occ} \\ a \in \text{virt}}} \theta_a^i a_a^\dagger a_i, \quad T_2 = \sum_{\substack{i > j \in \text{occ} \\ a > b \in \text{virt}}} \theta_{ab}^{ij} a_a^\dagger a_b^\dagger a_i a_j,$$

where occ and virt denote occupied and unoccupied orbitals in the reference state $|\psi_0\rangle$. Physically, the action of the UCC operator allows one to transfer “some amplitude” from initially occupied orbitals to the unoccupied ones. For real Hermitian Hamiltonians, the coefficients in (33) are real.

We would now like to translate (33), which was written in terms of the fermionic operators, into its qubit representation. According to the JW transformation [56], the qubit operators are obtained as

$$a_j^\dagger a_1 - a_1^\dagger a_j \mapsto \frac{i}{2} Y_1 Z_2 \dots Z_{j-1} X_j - \frac{i}{2} X_1 Z_2 \dots Z_{j-1} Y_j, \quad (34)$$

where X_i, Y_i, Z_i are the Pauli matrices acting on qubit i . Substituting (34) into (33) generates a mapping:

$$U(\vec{\theta}) \mapsto e^{i \sum_j \alpha_j P_j}, \quad (35)$$

where P_j are the Pauli operators, while α_j are the corresponding real coefficients. Trotterization of the expression above leads to

$$U(\vec{\theta}) \mapsto \left(\prod_j e^{i \frac{\alpha_j}{\rho} P_j} \right)^\rho, \quad (36)$$

where ρ is the Trotter number, which can be typically chosen quite small in VQE [67], unlike the case of simulating time evolution.

The traditional approach to calculating the expectation value as in (30) amounts to expanding the Hamiltonian in the basis of Pauli operators using (34):

$$\langle \psi(\vec{\theta}) | \hat{H} | \psi(\vec{\theta}) \rangle = \sum_i h_i \langle \psi(\vec{\theta}) | P_i | \psi(\vec{\theta}) \rangle. \quad (37)$$

The expectation values of individual Pauli terms on the RHS of (37) can be efficiently measured via sampling from the state $|\psi(\vec{\theta})\rangle$ [53].

The optimal parameters $\vec{\theta}^*$, obtained upon successful termination of the VQE algorithm, allow one to prepare the VQE approximation to the ground state of the system. By analogy with (37), this can be used to calculate the expectation value of any observable bilinear in the wave function (*i.e.*, of the form $\langle \psi(\vec{\theta}) | \hat{O} | \psi(\vec{\theta}) \rangle$), such as mass radius, PDF, or elastic form factor. Observables linear in the wave function (*i.e.*, of the form $|\langle v | \psi(\vec{\theta}) \rangle|$, where $|v\rangle$ is a constant vector), such as the decay constant, eq. (15b), can be calculated using the simple circuit shown in Fig. 2.

Efficiency analysis

When proposing new algorithms for quantum simulations on NISQ devices, it is essential to elicit their scaling properties in order to distinguish aspects of a particular simulation that may lead to quantum advantage from those that cannot. The question relevant to the present paper is which aspects of the few-qubit calculations we can scale up to several hundred qubits. Concomitantly, which aspects of the few-qubit calculations are amenable to efficient classical calculations and which are not.

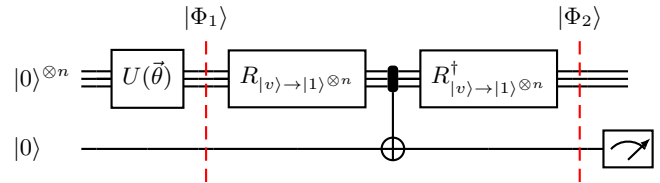


Figure 2. Estimating the magnitude of the inner product $\langle v | \psi(\vec{\theta}) \rangle$ for fixed $|v\rangle$. Up to the first dashed line, the circuit prepares the VQE ansatz state by applying the circuit $U(\vec{\theta})$ to the first set of registers, resulting in the state $|\Phi_1\rangle = |\psi(\vec{\theta})\rangle \otimes |0\rangle$. The next rotation, $R_{|v\rangle \rightarrow |1\rangle^{\otimes n}}$, represents any unitary operator that maps the state $|v\rangle$ to the state $|1\rangle^{\otimes n}$. Thus the state $|\Phi_2\rangle$ at the second dashed line is given by $|\Phi_2\rangle = \langle v | \psi(\vec{\theta}) \rangle |v\rangle \otimes |1\rangle + (|\psi(\vec{\theta})\rangle - \langle v | \psi(\vec{\theta}) \rangle |v\rangle) \otimes |0\rangle$.

The quantity $|\langle v | \psi(\vec{\theta}) \rangle| = \sqrt{|\langle v | \psi(\vec{\theta}) \rangle|^2}$ is found as the square root of the probability for the ancilla qubit to collapse into the state $|1\rangle$.

The stages of one shot of a VQE calculation are ansatz preparation and measurement of all Hamiltonian terms. Many shots with fixed ansatz parameters are required to obtain one estimate of the expectation value of the Hamiltonian. Many estimations of the expectation value of the Hamiltonian are required to optimize the ansatz parameters. Typically the resources required to optimize a given VQE ansatz to a fixed precision cannot be bounded theoretically. This is what makes VQE a heuristic method. However we can determine the computational cost of each step in a single shot and ensure that the quantum gates and qubits required scale polynomially with the problem size. We can also be sure that no known efficient classical algorithm exists for large-scale versions of the problem.

As a prototypical example, consider the problem of finding a ground state in quantum chemistry using VQE. The parameters describing the complexity of the problem are the total number of orbitals, N , and the number of electrons in the system, M (*i.e.*, the number of occupied orbitals). Using the direct mapping requires N qubits for encoding physical states. The second-quantized Hamiltonian operator can be written as a polynomial in ladder operators. Those, in turn, are each represented by a polynomial number of Pauli operators, each of which is at most $\log N$ -local. Therefore, the measurement of the Hamiltonian operator can be replaced with the measurement of a polynomial number of elementary operators. Each of those can be measured with precision ϵ using $O(\epsilon^{-2})$ samples [53, 68].

All that remains is to quantify the operational resources for preparing the ansätze. In quantum chemistry in the direct mapping, these are typically prepared using a unitary coupled cluster (UCC) operator. The UCC ansatz operator including single and double excitations (UCCSD) contains $O(N^2 M^2)$ free parameters. Application of the (trotterized) ansatz operator to the initial state is realized by a circuit containing a polynomial number of gates, since the action of fermionic ladder operators can be represented by a polynomial number of gates in the case of direct encoding.

Let us now see how these arguments can be naturally extended to the case of quantum field theory (QFT). First of all, we note that unlike in quantum chemistry, where the number of particles is conserved, QFT allows for processes of creation and annihilation of particles. Nevertheless, QFT does have an operator similar to the non-relativistic number operator — namely, the total momentum operator. Indeed, since this relativistic momentum operator commutes with the Hamiltonian, one can solve the problem within a Fock space sector of a fixed total momentum.

This analogy extends to the terms in the Hamiltonian. In quantum chemistry, the Hamiltonian operator can be written as a polynomial of fermionic creation and annihilation operators, containing $O(\text{poly}(N))$ terms. In QFT, the second-quantized Hamiltonian operator can be written as a polynomial of ladder operators, containing $O(\text{poly}(\Lambda))$ terms, where Λ is the momentum cutoff. As in chemistry, in the direct encoding those can be represented by $\log \Lambda$ -local Pauli operators, whose total number consequently also scales as $O(\text{poly}(\Lambda))$. To obtain a finite-dimensional Hilbert space in the equal time quantization, one would have to impose an additional cutoff on the number of excitations in each bosonic mode. However, in the LF formalism the maximum number of excitations is automatically limited by *harmonic resolution* K , the dimensionless light-cone momentum [33, 69]. Within the BLFQ, the role of Λ and K is played by N_{\max} , M_{\max} , and L_{\max} cutoffs (introduced in Sec. II C). Therefore, all the resources for a single VQE estimation of the QFT Hamiltonian expectation value based on the direct encoding and UCC will grow polynomially in momentum cutoffs and precision.

B. Compact encoding

In our previous work [33] we explored the possibility of using the compact encoding for simulating

physics on the light front. This amounts to only storing information about occupied modes in the Fock states. In the simplified setting considered in Sec. II B, due to the usage of relative coordinates, the only information we store is the index of the single occupied orbital. While in the direct mapping the index of the occupied orbital was stored in the unary form, requiring N qubits for N orbitals, in the compact mapping it is stored in the binary form, requiring $\lceil \log_2 N \rceil$ qubits for N orbitals. Therefore, in the case when the single-body Hamiltonian matrix h_{ij} is of size $N \times N = 2^n \times 2^n$, one would use all the basis states of the 2^n -dimensional Hilbert space of n qubits (see Table II).

In the compact mapping, an equation analogous to (34) would contain an exponential number of terms on the RHS, thus making the usage of the UCC inefficient. Instead, one may employ any of existing arbitrary state preparation algorithms [70]. While their complexity is exponential in the number of qubits, in our case the number of qubits is itself logarithmic in the problem cutoffs.

For the direct encoding, in order to measure the expectation value of the Hamiltonian we can express the Hamiltonian in terms of Pauli operators. Any observable of size $N \times N = 2^n \times 2^n$ can be expanded in the basis of $4^n = N^2$ Pauli operators defined on n qubits:

$$h = \sum_{\alpha=1}^{N^2} c_{\alpha} P_{\alpha}, \quad c_{\alpha} = \frac{1}{2^n} \text{tr}(h P_{\alpha}). \quad (38)$$

where c_{α} are *real*.

It should be emphasized that the logarithmic scaling of the number of qubits required as a function of the problem cutoffs implies that the Hilbert space dimension is polynomial in the cutoffs. This also implies that classical approaches to this problem are efficient. We are considering these specific initial problems as benchmarks where the results obtained can be compared to the known classical solution as an evaluation of the NISQ device itself.

Efficiency analysis

Within the VQE regime, the approach to quantum simulation based on the compact mapping is more efficient than the one based on the direct encoding when solving a two-body problem in the relative variable basis. As one starts to consider the problem in the multi-particle setting, the number of qubits required for storing physical states in the compact encoding is nearly optimal [33]. Despite that, one

faces serious problems at the stages of state preparation and measurement. Since the complexity of arbitrary state preparation algorithms scales exponentially with the number of qubits, and the number of qubits grows linearly with the number of occupied modes, those algorithms can only be used if the number of particles is fixed and small. Of course, in principle, one could use sparsity-based techniques for state preparation, but this produces gate counts that are not feasible in the NISQ era. Therefore, coming up with a good ansatz for a multi-particle state in the compact encoding is an important task, which we leave for future work.

Another problem arises at the measurement stage: the number of Pauli terms in the expansion of the Hamiltonian grows exponentially with the number of qubits. This motivates the development of VQE techniques for sparse Hamiltonians.

V. RESULTS

In this section we describe numerical and experimental results of implementing VQE for a sample QFT problem, namely simulation of a pion in the minimal BLFQ representation. In order to run our simulation on an existing device, we shall use the 4×4 light meson BLFQ Hamiltonian from Sec. II B corresponding to $J_z = 0$ sector in Table V (see also App. A 2):

$$h_{ij} = H^{\text{BLFQ}} = \begin{pmatrix} 640323 & 139872 & -139872 & -107450 \\ 139872 & 346707 & 174794 & 139872 \\ -139872 & 174794 & 346707 & -139872 \\ -107450 & 139872 & -139872 & 640323 \end{pmatrix}, \quad (39)$$

in units of MeV^2 . The two lowest eigenvalues correspond to π and ρ meson squared masses: the ground state is $(0.34, -0.62, -0.62, 0.34)^T$, with $m_\pi^2 = 139.6^2 \text{ MeV}^2$.

We can analyze the VQE calculation in a few steps: a) Check that the classical optimizer is working correctly. To eliminate any errors arising due to sampling, we begin with evaluating the Hamiltonian expectation values exactly, using the statevector representation. b) Determine the number of steps required to reach the desired precision when evaluating the expectation value via sampling from the exact distribution. This gives the lower bound on the number of samples, and models the situation of using a “perfect quantum computer.” c) Evaluate expectation values on the IBM Vigo quantum processor. d) Use error mitigation techniques to postpro-

cess the results obtained on the quantum computer. We shall perform these steps using both the direct and compact encodings, evaluating the Hamiltonian eigenstate as well as other observables discussed in Sec. III.

The multi-qubit states representing the four physical basis states are shown in Table II. The states in the direct encoding can be thought of as JW-encoded states. Therefore, we use the JW transformation for calculating the corresponding multi-qubit Hamiltonian:

$$H_{\text{direct}}^{\text{BLFQ}} = 987031IIII + 87397(IXXI + IYYI) - 53725(YZZY + XZZX) - 320161(IIIZ + ZIII) - 173353(IZII + IIZI) + 69936(IIYY + IIXX + YZYI + XZXI - IYZY - IXZX - YYII - XXII), \quad (40)$$

where each term is a tensor product of single-qubit Pauli matrices I, X, Y, Z . (In what follows, we use this convention when expanding Hermitian matrices in Pauli terms acting on qubits.)

As an ansatz operator, one could use the UCCS (no Doubles) operator. According to (33), T_1 will contain N terms, each of which is N -local in the JW encoding and $\log N$ -local in the BK encoding. In the former case, the circuit will contain $O(N^2)$ gates, while in the latter only $O(N \log N)$ gates. However, in order to further improve the gate count in the direct encoding-based algorithm, instead of the UCCS ansatz, we design a simple parametrized circuit of depth $O(\log N)$ using $O(N)$ gates shown in Fig. 3a, which is capable of preparing an arbitrary superposition (with real amplitudes) of single-occupied states in the JW encoding. (This circuit is a generalization of the circuit proposed in [71] for preparing W_N states.)

The multi-qubit representation of the Hamiltonian in the compact encoding is obtained from (39), calculating the coefficients by applying (38):

$$H = 33671XX + 141122YY + 146807ZZ + 493515II + 139872(ZX - XZ). \quad (41)$$

The ansatz state is prepared using the circuit shown in Fig. 3b, which prepares an arbitrary two-qubit state with real amplitudes. For both encodings, we need to estimate expectation values of Pauli operators. To do this, we first rotate to a basis in which the desired Pauli operator is diagonal, then measure single-qubit Z operators. The desired operator is a product of some set of single-qubit Z operators in this basis.

\mathbf{m}	$\overline{\mathbf{m}}$	κ	G_π	N_{\max}	M_{\max}	L_{\max}
337.01 MeV	337.01 MeV	227.00 MeV	250.785 GeV ⁻²	0	2	0

Table III. Model parameters for the BLFQ-NJL model.

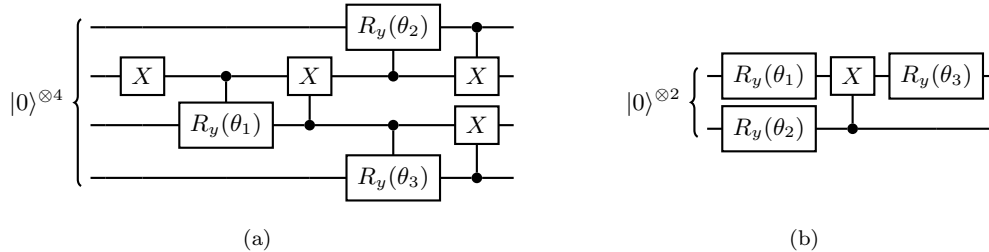


Figure 3. Ansatz circuits for preparing an arbitrary superposition of single-particle Fock states with real coefficients. For the direct encoding (a), we use a generalization of a circuit from [71] for preparation of W_N states. For the binary encoding (b), we use arbitrary state preparation, with all single qubit rotations replaced by $R_y(\theta)$ gates, where $R_y(\theta)$ denotes a single-qubit rotation through an angle θ about the y -axis.

The classical optimization was performed using various algorithms from the `python.scipy.optimize` library. In agreement with [54], the best convergence to the true ground state was achieved with L-BFGS-B [72] and COBYLA [73] methods. The latter showed better convergence, and it is used in all the following calculations. Depending on the choice of the initial guess state, the optimizer was typically reaching 4-digit precision after $\sim 10^1$ - 10^2 steps (for a good initial guess, such as $(0, -1/\sqrt{2}, 1/\sqrt{2}, 0)^T$) and up to a few hundred steps for randomly chosen initial state. In rare cases, the minimization was not converging.

Next, we determined the number of samples from the exact distribution required to reach the desired precision, which is expected to scale as $O(1/\epsilon^2)$ [68]. To do so, we calculated the relative error for determining the Hamiltonian's expectation value in the true ground state using the classical simulation (the corresponding parameters of the circuits were obtained via the optimization at the previous stage). We performed 1000 experiments with a fixed number of samples, and calculated the RMS relative errors in determining the ground state expectation value over each set of experiments. The results on Fig. 4 indicate that on an ideal quantum computer we would need to generate $\sim 10^6$ samples per Pauli term in order to reach 2% precision, and $\sim 4 \cdot 10^6$ samples to reach 1% precision.

Fig. 7 shows the relative errors for the energy, decay constant, and mass radius, evaluated in the approximate ground state obtained via the VQE minimization procedure. The expressions for all observ-

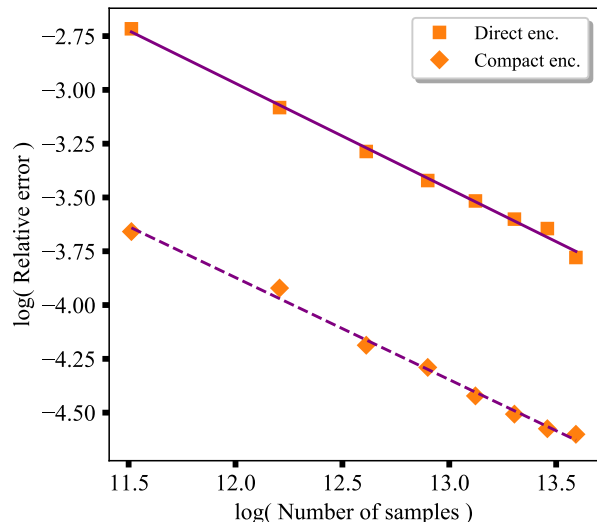


Figure 4. Precision vs. number of samples for ground state energy obtained via sampling from the exact distribution. Fitting gives $n \approx 382/\epsilon^{2.04}$ (direct encoding) and $n \approx 46/\epsilon^{2.1}$ in (compact encoding), confirming the theoretical $n \sim O(1/\epsilon^2)$ dependence. Compact encoding shows better convergence due to having shorter circuits on fewer qubits (compare Figs. 3a and 3b).

ables are obtained from the corresponding BLFQ matrices in analogy with eqs. (40) and (41); the explicit expressions can be found in App. D. Note that all the observables have a dominant contribution from the unity term ($IIII$ in the direct encoding and II in the compact encoding), whose expectation value is exactly 1. Therefore, in Fig. 7 we also show

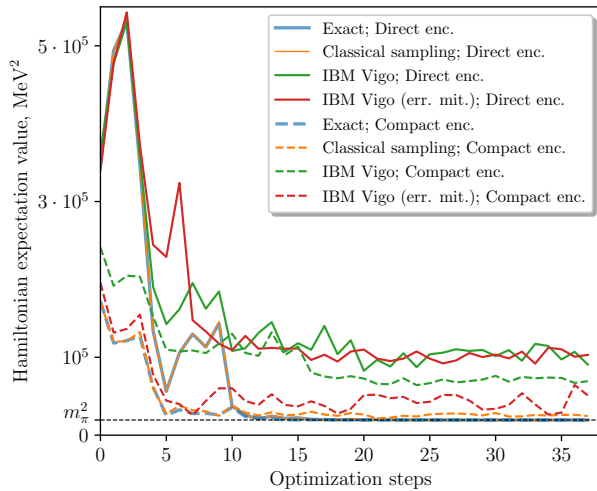


Figure 5. The results of the VQE minimization algorithm in the compact and direct encodings. These were obtained from 8192 samples per term on IBM Vigo machine, with and without measurement error mitigation.

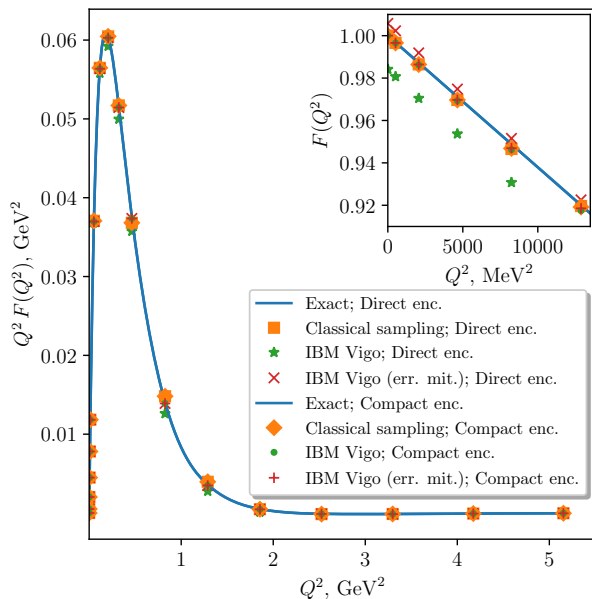


Figure 6. Pion elastic form factor, as defined in eq. (27). Pion elastic form factor is used to calculate the charge radius, obtaining the values given in Tab. IV (charge radius is defined in eq. 28). Datapoints for the quantum simulation on the IBM Vigo processor used 8192 samples per term, with and without measurement error mitigation. The results measured on the quantum computer are in good agreement with the exact ones due to the strong contribution to the measurement operators from the identity term.

the expectation values for observables from which this term has been subtracted, which in certain cases improves the relative precision of results. The expectation values without the unit terms are the quantities actually measured on the quantum computer, while those including the unit terms are the physically relevant numbers, so the relative errors in both are of interest. In order to calculate the decay constant, one can use the circuit shown in Fig. 2 or Pauli measurements; we use the latter option to minimize the number of gates.

The elastic form factors, eq. (27), are shown in Fig. 6, and the corresponding charge radii, eq. (28), are presented in the Table IV. In both cases, the results obtained on the quantum computer are in good agreement with the exact ones. This is to be expected, because the corresponding measurement operators have a large contribution from the identity operator.

With our choice of cutoffs, the calculation of PDFs in the compact encoding reduces to measurement of II , while in the direct encoding, it reduces to the projector onto the computational subspace (spanned by the single-occupancy Fock states). Thus in both cases, the quantity to be measured on the quantum computer is trivial (*i.e.*, $\rho_{0,0} = 1$, as in eq. (23)), and the resulting PDF is $f(x) = \rho_{0,0} \chi_0^2(x) = 1. \times (2986 x^{4.4} (1-x)^{4.4})^2$.

	Charge radius $\sqrt{\langle r_c^2 \rangle}$, MeV $^{-1}$	
Encoding	Direct	Compact
Exact	$6.31 \cdot 10^{-3}$	$6.31 \cdot 10^{-3}$
Classical sampling	$6.29 \cdot 10^{-3}$	$6.30 \cdot 10^{-3}$
IBM Vigo	$6.33 \cdot 10^{-3}$	$6.35 \cdot 10^{-3}$
IBM Vigo (err. mit.)	$6.34 \cdot 10^{-3}$	$6.31 \cdot 10^{-3}$

Table IV. Pion charge radius, as defined in eq. (28), calculated using the numerical results from Fig. 6.

VI. DISCUSSION

In our paper, for the first time we simulated high energy nuclear physics in the light front formulation on existing devices. We considered a detailed example in which we studied a relativistic analog of hydrogen, the pion. We studied this problem in a fixed particle number formulation as a benchmarking test for existing devices, and as a preparation for moving on to the mixed particle number formulation. Using the basis light front quantization (BLFQ) formalism, we demonstrated how small quantum computers can

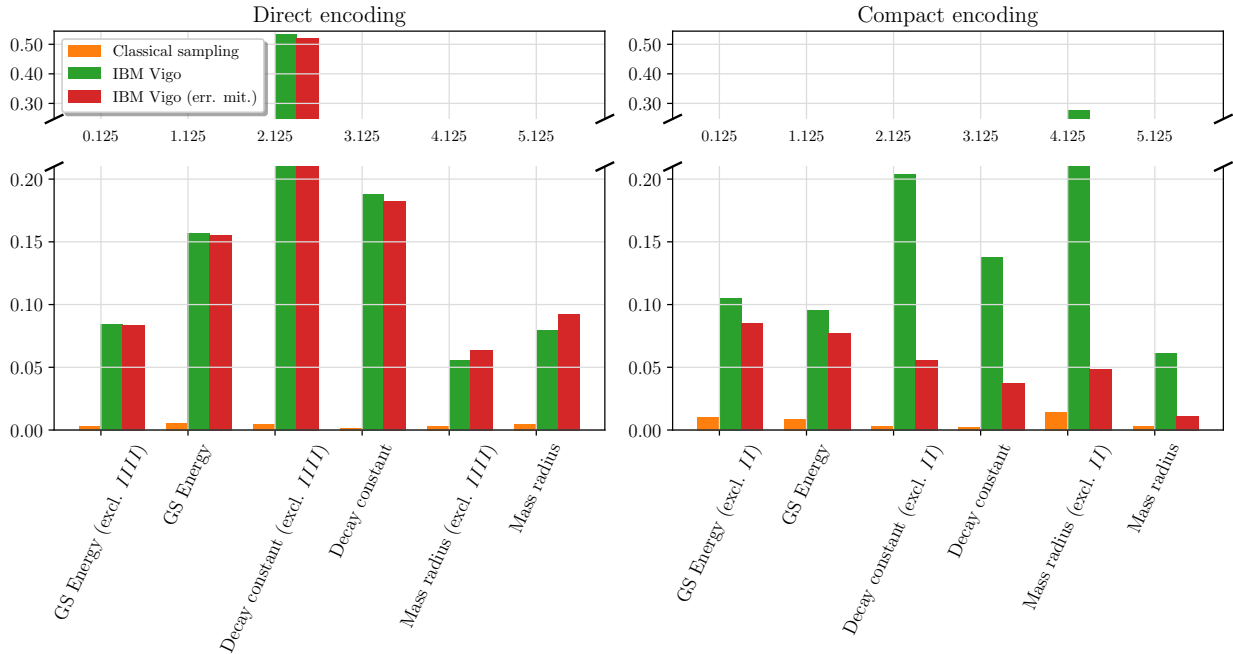


Figure 7. Relative errors in estimates of various observables. These were obtained from 8192 samples per term on IBM Vigo machine, with and without measurement error mitigation. Physically significant observables have a significant contribution from the constant term in their multi-qubit representation. Observables are shown with and without the contribution of the constant term. For the GS energy, the error was calculated relative to the second lowest eigenvalue, m_p^2 . For the compact encoding, measurement error mitigation consistently improves the results.

be used for calculating baryonic spectra and various observables. Adopting an effective interaction (suggested by AdS/QCD correspondence [74]) and a set of basis functions (motivated by the particular problem of interest [34]) allows one to significantly reduce the computational resources, and to obtain reasonable results for realistic theories on devices having just a few qubits.

Within the VQE approach to quantum simulation, studied in the present work, we considered various encodings and state preparation procedures, some of which were naturally suggested by our experience in quantum chemistry. Together with our previous paper [33], this work defines a spectrum of methods for quantum simulation of quantum field theories. On this spectrum, one can move from restricted models, to be simulated on existing quantum devices, all the way to full *ab initio* simulation of QCD in 3+1D, to be simulated on future fault-tolerant quantum computers. Future work will expand and improve our methods on both ends of the spectrum. The next step in near-term simulation will be to switch to single-particle coordinates, providing the framework for mixed particle number simulations where quan-

tum advantage is possible.

ACKNOWLEDGMENTS

W. M. K. acknowledges support from the National Science Foundation, Grant No. DGE-1842474. P. J. L., M. K. and G. G. acknowledge support from DOE HEP Grant No. DE-SC0019452. S. J. and J. P. V. acknowledge support from DOE Grant Nos. DE-FG02-87ER40371 and DE-SC0018223. S. J. also acknowledges support from DOE Office of Science, Office of Nuclear Physics, contract No. DE-AC02-06CH11357. This work was supported by the NSF STAQ project (PHY-1818914).

Appendix A: Hamiltonian in the basis representation

1. Unitary transformation to the fixed J_z blocks

Because the light-front Hamiltonian conserves the angular momentum in the z direction, the Hamiltonian in our basis representation can be diagonalized into blocks of fixed J_z . This is equivalent to combining the spin quantum numbers s_1 and s_2 with the magnetic quantum number m to form a new quantum number θ . Specifically when $M_{\max} = 2$, the unitary transformation from the original BLFQ basis to this block-diagonal form is given by Table V.

J_z	θ	m	s_1	s_2
-3	1	-2	-	-
-2	1	-2	+	-
-2	2	-2	-	+
-2	3	-1	-	-
-1	1	-2	+	+
-1	2	-1	+	-
-1	3	-1	-	+
-1	4	0	-	-
0	1	-1	+	+
0	2	0	+	-
0	3	0	-	+
0	4	1	-	-
1	1	0	+	+
1	2	1	+	-
1	3	1	-	+
1	4	2	-	-
2	1	1	+	+
2	2	2	+	-
2	3	2	-	+
3	1	2	+	+

Table V. The unitary transformation from the orthogonal enumeration to blocks with fixed J_z . The other basis quantum numbers n and l are identical in both representations. Here we only impose the basis cut-off of $M_{\max} = 2$, while cut-offs in l and n can be freely determined.

2. The BLFQ-NJL Hamiltonian in the $J_z = 0$ block

When $N_{\max} = L_{\max} = 0$, the light-front effective Hamiltonian in the $J_z = 0$ block takes the form of a 4-by-4 matrix. The subscripts of the matrix then index the basis quantum number θ . The explicit expressions for these matrix elements are given in

the following equations. Here κ is strength of the confining potential which we set identical to the basis scale b . The parameter G_π is the coupling constant of the NJL interaction. Functions $L'(a, b)$ and $L(a, b)$ both stand for $L_0(a, b; \alpha, \beta)$ given in Appendix B 3.

Explicitly, the matrix elements of this Hamiltonian in our basis representation is given by

$$H_{11} = (\mathbf{m} + \overline{\mathbf{m}})^2 + 5\kappa^2 + \frac{8G_\pi b^4}{\pi} L'(0, 0)L(0, 0), \quad (\text{A1a})$$

$$H_{12} = \frac{4G_\pi b^3}{\pi} \left\{ \mathbf{m} \{ [L'(0, 1)L(1/2, -1/2) - L'(0, 0)L(1/2, -1/2)] \right. \\ \left. + \overline{\mathbf{m}} L'(0, 0)L(-1/2, 1/2) \right\}, \quad (\text{A1b})$$

$$H_{13} = -\frac{2G_\pi b^3}{\pi} L'(0, 0) \left\{ \overline{\mathbf{m}} \{ 2L(-1/2, 1/2) + L(-1/2, 3/2) + L(1/2, 1/2) \} \right. \\ \left. + 2\mathbf{m} L(1/2, -1/2) \right\}, \quad (\text{A1c})$$

$$H_{14} = -\frac{4G_\pi b^4}{\pi} \{ L'(0, 1)L(1, 0) + L'(1, 0)L(0, 1) + L'(0, 1)L(0, 0) + L'(0, 0)L(0, 1) \\ - 2L'(0, 1)L(0, 1) + 2L'(0, 0)L(0, 0) \}, \quad (\text{A1d})$$

$$H_{21} = H_{12}, \quad (\text{A1e})$$

$$H_{22} = (\mathbf{m} + \overline{\mathbf{m}})^2 + 3\kappa^2 - \frac{G_\pi b^2}{\pi} \overline{\mathbf{m}}\mathbf{m} \\ \times \{ L'(1/2, 1/2)L(-1/2, -1/2) + L'(-1/2, 1/2)L(1/2, -1/2) \\ + L'(1/2, -1/2)L(-1/2, 1/2) + L'(-1/2, -1/2)L(1/2, 1/2) \\ + L'(-1/2, 3/2)L(-1/2, -1/2) - 2L'(-1/2, 1/2)L(-1/2, 1/2) \\ + L'(-1/2, -1/2)L(-1/2, 3/2) \} \quad (\text{A1f})$$

$$- \frac{2G_\pi b^2}{\pi} \{ \overline{\mathbf{m}} L'(-1/2, 1/2) + \mathbf{m} L'(1/2, -1/2) \} \{ \overline{\mathbf{m}} L(-1/2, 1/2) + \mathbf{m} L(1/2, -1/2) \} \\ H_{23} = \frac{2G_\pi b^2}{\pi} [\overline{\mathbf{m}} L'(-1/2, 1/2) + \mathbf{m} L'(1/2, -1/2)] \\ \times [\overline{\mathbf{m}} L(-1/2, 1/2) + \mathbf{m} L(1/2, -1/2)], \quad (\text{A1g})$$

$$\begin{aligned}
H_{24} &= \frac{2G_\pi b^3}{\pi} \bar{\mathbf{m}} \{ [L'(-1/2, 3/2) + 2L'(-1/2, 1/2)] \\
&\quad \times L(0, 0) - L'(-1/2, 1/2)L(0, 1) \} \\
&\quad + \frac{2G_\pi b^3}{\pi} \mathbf{m} \{ [L'(1/2, 1/2) + 2L'(1/2, -1/2)] \\
&\quad \times L(0, 0) + L'(1/2, -1/2)L(0, 1) \} , \tag{A1h}
\end{aligned}$$

$$H_{31} = H_{13} , \tag{A1i}$$

$$H_{32} = H_{23} , \tag{A1j}$$

$$\begin{aligned}
H_{33} &= (\mathbf{m} + \bar{\mathbf{m}})^2 + 3\kappa^2 - \frac{G_\pi b^2}{\pi} \bar{\mathbf{m}} \mathbf{m} \\
&\quad \times \{ L'(1/2, 1/2)L(-1/2, -1/2) \\
&\quad + L'(-1/2, 1/2)L(1/2, -1/2) \\
&\quad + L'(1/2, -1/2)L(-1/2, 1/2) \\
&\quad + L'(-1/2, -1/2)L(1/2, 1/2) \\
&\quad + L'(-1/2, 3/2)L(-1/2, -1/2) \\
&\quad - 2L'(-1/2, 1/2)L(-1/2, 1/2) \\
&\quad + L'(-1/2, -1/2)L(-1/2, 3/2) \} \tag{A1k}
\end{aligned}$$

$$\begin{aligned}
&\quad - \frac{2G_\pi b^2}{\pi} [\bar{\mathbf{m}} L'(-1/2, 1/2) + \mathbf{m} L'(1/2, -1/2)] \\
&\quad \quad \times [\bar{\mathbf{m}} L(-1/2, 1/2) + \mathbf{m} L(1/2, -1/2)] , \\
H_{34} &= -\frac{4G_\pi b^3}{\pi} \left\{ \mathbf{m} \{ L'(1/2, -1/2)L(0, 1) \right. \\
&\quad \quad + L'(1/2, -1/2)L(0, 0) \} \tag{A1l} \\
&\quad \quad \left. + \bar{\mathbf{m}} L'(-1/2, 1/2)L(0, 0) \right\} ,
\end{aligned}$$

$$H_{41} = H_{14} , \tag{A1m}$$

$$H_{42} = H_{24} , \tag{A1n}$$

$$H_{43} = H_{34} , \tag{A1o}$$

$$\begin{aligned}
H_{44} &= (\mathbf{m} + \bar{\mathbf{m}})^2 + 5\kappa^2 \\
&\quad - \frac{8G_\pi b^4}{\pi} L'(0, 0)L(0, 0) . \tag{A1p}
\end{aligned}$$

Appendix B: Analytical expressions for integrals of basis functions

1. Integrals for the calculation of the decay constant

When calculating the decay constants using the valence LFWFs of mesons, we encounter the follow-

ing integral:

$$\begin{aligned}
&\int_0^1 \frac{dx}{4\pi\sqrt{x(1-x)}} \int \frac{d^2\kappa^\perp}{(2\pi)^2} \phi_{nm} \left(\frac{\vec{\kappa}^\perp}{\sqrt{x(1-x)}} \right) \chi_l(x) \\
&= \int_0^{2\pi} \frac{d\phi}{2\pi} e^{im\phi} \int_0^1 \frac{dx}{4\pi} \sqrt{x(1-x)} \chi_l(x) \int \frac{\rho d\rho}{2\pi b} \\
&\quad \times \sqrt{\frac{4\pi n!}{(n+|m|)!}} \left(\frac{q}{b} \right)^{|m|} e^{-q^2/(2b^2)} L_n^{|m|}(q^2/b^2) q^{|m|} \\
&= \delta_{m,0} L_l(1/2, 1/2; \alpha, \beta) \frac{b}{\sqrt{\pi}} (-1)^n , \tag{B1}
\end{aligned}$$

where $L_l(1/2, 1/2; \alpha, \beta)$ is given by Eq. (B7). We have also used

$$\int_0^{+\infty} \frac{q dq}{2\pi b} \sqrt{4\pi} e^{-q^2/(2b^2)} L_n^0(q^2/b^2) = \frac{b}{\sqrt{\pi}} (-1)^n \tag{B2}$$

in deriving Eq. (B1).

2. Integrals for the mass radius

To evaluate the transverse integrals in Eq. (21), we first define $\vec{\rho} = b\sqrt{x(1-x)}\vec{r}^\perp$. After this substitution of variables we obtain

$$\begin{aligned}
&\int_0^{+\infty} d|\vec{r}^\perp|^2 \int_0^{2\pi} \frac{d\phi_r}{2} x^2(1-x)^2 b^2 |\vec{r}^\perp|^2 \\
&\quad \times \tilde{\phi}_{n',m'}^* \left(\sqrt{x(1-x)}\vec{r}^\perp \right) \tilde{\phi}_{n,m} \left(\sqrt{x(1-x)}\vec{r}^\perp \right) \\
&= b^{-2} \int_0^{+\infty} d\rho^2 \int_0^{2\pi} \frac{d\phi_r}{2} \rho^2 \tilde{\phi}_{n',m'}^* \left(\vec{\rho}^\perp/b \right) \\
&\quad \times \tilde{\phi}_{n,m} \left(\vec{\rho}^\perp/b \right) \tag{B3} \\
&= (-1)^{n'+n} \delta_{m'm} \sqrt{\frac{n'!n!}{(n'+|m|)!(n+|m|)!}} \\
&\quad \times \int_0^{+\infty} d\rho^2 (\rho^2)^{|m|+1} e^{-\rho^2} L_{n'}^{|m|}(\rho^2) L_n^{|m|}(\rho^2) .
\end{aligned}$$

The integrals over the product of generalized Laguerre polynomials can be obtained by the orthonormality relations. In order to apply such relations, we convert $L_n^{|m|}$ into $L_n^{|m|+1}$ using recurrence relations. From Eq. (22.7.30) of Ref. [75] we obtain

$$L_n^{|m|}(\rho^2) = L_n^{|m|+1}(\rho^2) - L_{n-1}^{|m|+1}(\rho^2) . \tag{B4}$$

Here when $n = 0$, the second term drops out. We then have

$$\begin{aligned}
& \sqrt{\frac{n'!n!}{(n'+|m|)!(n+|m|)!}} \\
& \times \int_0^{+\infty} d\rho^2 (\rho^2)^{|m|+1} e^{-\rho^2} L_{n'}^{|m|}(\rho^2) L_n^{|m|}(\rho^2) \\
& = \sqrt{\frac{n'!n!}{(n'+|m|)!(n+|m|)!}} \int_0^{+\infty} d\rho^2 (\rho^2)^{|m|+1} e^{-\rho^2} \\
& \times \left[L_{n'}^{|m|+1}(\rho^2) - \theta_{n'-1} L_{n'-1}^{|m|+1}(\rho^2) \right] \\
& \times \left[L_n^{|m|+1}(\rho^2) - \theta_{n-1} L_{n-1}^{|m|+1}(\rho^2) \right] \quad (\text{B5}) \\
& = \sqrt{\frac{n'!n!}{(n'+|m|)!(n+|m|)!}} \left\{ \frac{(n+|m|+1)!}{n!} \delta_{n'n} \right. \\
& - \frac{(n+|m|)!}{(n-1)!} \delta_{n',n-1} \theta_{n-1} - \frac{(n+|m|+1)!}{n!} \delta_{n',n+1} \\
& \left. + \frac{(n+|m|)!}{(n-1)!} \delta_{n'n} \theta_{n-1} \right\} \\
& = (2n+|m|+1) \delta_{n'n} - \sqrt{n(n+|m|)} \delta_{n',n-1} \\
& - \sqrt{(n+1)(n+|m|+1)} \delta_{n',n+1} .
\end{aligned}$$

with $n \in \mathbf{N}$ by default.

The longitudinal integrals can be calculated by applying the orthonormal relation of the longitudinal basis function. Subsequently, we obtain the following expression for the hermitian matrix that specifies the mass radius:

$$\begin{aligned}
& I_m(n', m', l'; n, m, l) \\
& = \delta_{l'l} \delta_{m'm} \left\{ (2n+|m|+1) \delta_{n'n} \right. \\
& + \sqrt{n(n+|m|)} \delta_{n',n-1} \\
& \left. + \sqrt{(n+1)(n+|m|+1)} \delta_{n',n+1} \right\} . \quad (\text{B6})
\end{aligned}$$

3. Longitudinal integrals

Let us define the following integral in the longitudinal basis functions:

$$\begin{aligned}
& L_l(a, b; \alpha, \beta) \\
& \equiv \int_0^1 \frac{dx}{4\pi} x^b (1-x)^a \chi_l(x; \alpha, \beta) \\
& = \sqrt{\frac{2l+\alpha+\beta+1}{4\pi}} \sqrt{\frac{\Gamma(l+1)\Gamma(l+\alpha+\beta+1)}{\Gamma(l+\alpha+1)\Gamma(l+\beta+1)}} \\
& \times \int_0^1 dx x^{\beta/2+b} (1-x)^{\alpha/2+a} P_l^{(\alpha, \beta)}(2x-1) \\
& = \sqrt{\frac{2l+\alpha+\beta+1}{4\pi}} \sqrt{\frac{\Gamma(l+1)\Gamma(l+\alpha+\beta+1)}{\Gamma(l+\alpha+1)\Gamma(l+\beta+1)}} \\
& \times \sum_{m=0}^l \binom{l+\alpha}{m} \binom{l+\beta}{l-m} (-1)^{l-m} \quad (\text{B7}) \\
& \times B\left(\frac{\beta}{2} + b + m + 1, \frac{\alpha}{2} + a + l - m + 1\right),
\end{aligned}$$

where $B(s, t) = \Gamma(s)\Gamma(t)/\Gamma(s+t)$ is the Euler Beta function.

To evaluate $L_l(a, b; \alpha, \beta)$ numerically, we first rewrite Eq. (B7) as

$$\begin{aligned}
& L_l(a, b; \alpha, \beta) = \sqrt{\frac{2l+\alpha+\beta+1}{4\pi}} \\
& \times \sum_{m=0}^l C_{l,m}(a, b; \alpha, \beta), \quad (\text{B8})
\end{aligned}$$

with

$$\begin{aligned}
& C_{l,m} \equiv \frac{(-1)^{l-m} \sqrt{\Gamma(l+1)\Gamma(l+\alpha+\beta+1)}}{\Gamma(m+1)\Gamma(l+\alpha-m+1)} \\
& \times \frac{\sqrt{\Gamma(l+\alpha+1)\Gamma(l+\beta+1)}}{\Gamma(l-m+1)\Gamma(\beta+m+1)} \quad (\text{B9}) \\
& \times \frac{\Gamma(\beta/2+b+m+1)\Gamma(\alpha/2+a+l-m+1)}{\Gamma(\beta/2+b+\alpha/2+a+l+2)}.
\end{aligned}$$

We then obtain the following recurrence relations for $C_{l,m}$:

$$\begin{aligned}
& C_{0,0} = \sqrt{\frac{\Gamma(\alpha+\beta+1)}{\Gamma(\alpha+1)\Gamma(\beta+1)}} \\
& \times \frac{\Gamma(\beta/2+b+1)\Gamma(\alpha/2+a+1)}{\Gamma(\beta/2+b+\alpha/2+a+2)}, \quad (\text{B10a})
\end{aligned}$$

$$\begin{aligned}
& \frac{C_{l,0}}{C_{l-1,0}} = -\sqrt{\frac{(l+\beta)(l+\alpha+\beta)}{l(l+\alpha)}} \\
& \times \frac{\alpha/2+a+l}{\beta/2+b+\alpha/2+a+l+1} \quad (\text{for } l \geq 1), \quad (\text{B10b})
\end{aligned}$$

$$\frac{C_{l,m}}{C_{l,m-1}} = -\frac{(l+\alpha-m+1)(l-m+1)}{m(\beta+m)(\alpha/2+a+l-m+1)} \times (\beta/2+b+m) \quad (\text{for } l \geq m \geq 1). \quad (\text{B10c})$$

The longitudinal integral $L_l(a, b; \alpha, \beta)$ can then be calculated by first generating and then summing the following sequences:

$$\begin{array}{c} C_{0,0} \\ \downarrow \\ C_{1,0} + C_{1,1} \\ \downarrow \\ C_{2,0} + C_{2,1} + C_{2,2} \\ \downarrow \\ C_{3,0} + C_{3,1} + C_{3,2} + C_{3,3} \\ \downarrow \\ \dots \end{array},$$

using Eq. (B10).

Appendix C: The electromagnetic form factors in the basis representation

1. Reduction of the formula for the electromagnetic form factors in the valence Fock sector of mesons

Let us first expand the quark current operator in terms of creation and annihilation operators. In agreement with the light-front quantization condition, the Dirac field operator at a given light-front time $x^+ = 0$ is expanded according to

$$\begin{aligned} \psi(x) &= \sum_{s=\pm 1/2} \int d\underline{p} \\ &\times \left[b_s(p) u_s(p) e^{-ip \cdot x} + d_s^\dagger(p) v_s(p) e^{ip \cdot x} \right] \Big|_{x^+=0}, \end{aligned} \quad (\text{C1})$$

where the flavor indices are implicit. Here $u_s(p)$ and $v_s(p)$ are solutions of the Dirac equation for free fermions. Meanwhile, the creation and annihilation operators satisfy these anti-commutation relations:

$$\{b_r(k), b_s^\dagger(p)\} = \underline{\delta}(k-p) \delta_{rs}, \quad (\text{C2})$$

$$\{d_r(k), d_s^\dagger(p)\} = \underline{\delta}(k-p) \delta_{rs}, \quad (\text{C3})$$

while other anti-commutation relations all vanish. We have defined the integral measure in the momentum space as

$$\int d\underline{p} = \int_0^{+\infty} \frac{dp^+}{4\pi p^+} \int_{-\infty}^{+\infty} \frac{dp_1^\perp}{2\pi} \int_{-\infty}^{+\infty} \frac{dp_2^\perp}{2\pi}. \quad (\text{C4})$$

The reduced delta-function is defined according to

$$\begin{aligned} \underline{\delta}(k-p) &= 4\pi k^+ \theta(k^+) \delta(k^+ - p^+) \\ &\times (2\pi)^2 \delta(\vec{k}^\perp - \vec{p}^\perp). \end{aligned} \quad (\text{C5})$$

These conventions ensure that one reduced delta-function can be utilized to eliminate one momentum-space integration.

With these definitions, the charge density operator becomes

$$\begin{aligned} \lim_{x \rightarrow 0} e_f \psi(x) \gamma^+ \psi(x) &= \lim_{x \rightarrow 0} \sum_{s's} \int d\underline{p}' \int d\underline{p} \\ &\times \left[b_{s'}^\dagger(p') \bar{u}_{s'}(p') e^{ip' \cdot x} + d_{s'}(p') \bar{v}_{s'}(p') e^{-ip \cdot x} \right] \\ &\times e_f \gamma^+ \left[b_s(p) u_s(p) e^{-ip \cdot x} + d_s^\dagger(p) v_s(p) e^{ip \cdot x} \right] \\ &\rightarrow \sum_{s's} \int d\underline{p}' \int d\underline{p} \left\{ e_q b_{s'}^\dagger(p') b_s(p) \bar{u}_{s'}(p') \gamma^+ u_s(p) \right. \\ &\quad \left. - e_q d_{s'}^\dagger(p') d_s(p) \bar{v}_{s'}(p') \gamma^+ v_s(p) \right\} \\ &= \sum_s \int d\underline{p}' \int d\underline{p} 2\sqrt{p'^+ p^+} \\ &\quad \left[e_q b_s^\dagger(p') b_s(p) - e_q d_s^\dagger(p') d_s(p) \right]. \end{aligned} \quad (\text{C6})$$

Here we have made use of $\bar{u}_{s'}(p') \gamma^+ u_s(p) = 2\sqrt{p'^+ p^+} \delta_{s's}$ and $\bar{v}_{s'}(p') \gamma^+ v_s(p) = 2\sqrt{p'^+ p^+} \delta_{s's}$. We have only kept terms of relevance to the valence Fock sector of mesons. The form factors then becomes

$$\begin{aligned} &I_{m'_J, m_J}(Q^2) \\ &= \sum_{r's'} \int_0^1 \frac{dx'}{4\pi x'(1-x')} \int \frac{d\vec{k}'^\perp}{(2\pi)^2} \psi_{r's'}^*(x', \vec{k}'^\perp) \\ &\times \langle 0 | d_{s'}(k'_2) b_{r'}(k'_1) \sum_\sigma \int d\underline{p}' \int d\underline{p} \\ &\times \frac{\sqrt{p'^+ p^+}}{P^+} \left[e_q b_\sigma^\dagger(p') b_\sigma(p) - e_q d_\sigma^\dagger(p') d_\sigma(p) \right] \\ &\times \sum_{rs} \int_0^1 \frac{dx}{4\pi x(1-x)} \int \frac{d\vec{k}^\perp}{(2\pi)^2} \\ &\times b_r^\dagger(k_1) d_s^\dagger(k_2) |0\rangle \psi_{rs}(x, \vec{k}^\perp). \end{aligned} \quad (\text{C7})$$

The anti-commutation relation for the creation and annihilation operator can be used to deduce

$$\begin{aligned} &\sum_\sigma \int d\underline{p}' \int d\underline{p} d_{s'}(k'_2) b_{r'}(k'_1) b_\sigma^\dagger(p') b_\sigma(p) \\ &\times b_r^\dagger(k_1) d_s^\dagger(k) \sqrt{p'^+ p^+} \rightarrow \sqrt{k_1^+ k_1^+} \delta_{r'r} \delta_{s's} \underline{\delta}(k'_2 - k_2), \end{aligned} \quad (\text{C8})$$

$$\begin{aligned} & \sum_{\sigma} \int d\underline{p}' \int d\underline{p} d_{s'}(k'_2) b_{r'}(k'_1) d_{\sigma}^{\dagger}(p') d_{\sigma}(p) \quad (\text{C9}) \\ & \times b_r^{\dagger}(k_1) d_s^{\dagger}(k) \sqrt{p'^+ p^+} \rightarrow \sqrt{k_2'^+ k_2^+} \delta_{r'r} \delta_{s's} \underline{\delta}(k'_1 - k_1). \end{aligned}$$

The expression for the form factors is then reduced to

$$\begin{aligned} & I_{m',m_J}(Q^2) \\ & = \sum_{rs} \int \frac{dx'}{4\pi x'(1-x')} \int \frac{d\vec{k}^{\perp}}{(2\pi)^2} \psi_{rs}^*(x', \vec{k}^{\perp}) \\ & \times \int \frac{dx}{4\pi x(1-x)} \int \frac{d\vec{k}^{\perp}}{(2\pi)^2} \psi_{rs}(x, \vec{k}^{\perp}) \left\{ e_q \right. \\ & \times \left. \frac{\sqrt{k_1'^+ k_1^+}}{P^+} \underline{\delta}(k'_2 - k_2) - e_{\bar{q}} \frac{\sqrt{k_2'^+ k_2^+}}{P^+} \underline{\delta}(k'_1 - k_1) \right\}, \quad (\text{C10}) \end{aligned}$$

where we have defined

$$k_1^+ = xP^+, \quad (\text{C11a})$$

$$\vec{k}_1^{\perp} = \vec{k}^{\perp} + x\vec{P}^{\perp}, \quad (\text{C11b})$$

$$k_2^+ = (1-x)P^+, \quad (\text{C11c})$$

$$\vec{k}_2^{\perp} = -\vec{k}^{\perp} + (1-x)\vec{P}^{\perp}, \quad (\text{C11d})$$

and

$$k_1' = x'P'^+, \quad (\text{C11e})$$

$$\vec{k}_1'^{\perp} = \vec{k}'^{\perp} + x'\vec{P}'^{\perp} \quad (\text{C11f})$$

$$k_2'^+ = (1-x')P'^+, \quad (\text{C11g})$$

$$\vec{k}_2'^{\perp} = -\vec{k}'^{\perp} + (1-x')\vec{P}'^{\perp}. \quad (\text{C11h})$$

Meanwhile, the following reductions of delta-functions hold in the Drell-Yan frame:

$$\begin{aligned} \underline{\delta}(k'_2 - k_2) & = 4\pi(1-x)\delta(x' - x)(2\pi)^2 \\ & \times \delta^2 \left(-\vec{k}'^{\perp} + \vec{k}^{\perp} + (1-x)(\vec{P}'^{\perp} - \vec{P}^{\perp}) \right), \quad (\text{C12}) \end{aligned}$$

$$\begin{aligned} \underline{\delta}(k'_1 - k_1) & = 4\pi x \delta(x' - x)(2\pi)^2 \\ & \times \delta^2 \left(\vec{k}'^{\perp} - \vec{k}^{\perp} + x(\vec{P}'^{\perp} - \vec{P}^{\perp}) \right). \quad (\text{C13}) \end{aligned}$$

Therefore the expression for the form factors is reduced to that given on the right-hand side of Eq. (25) with $\vec{q}^{\perp} = \vec{P}'^{\perp} - \vec{P}^{\perp}$.

2. The electromagnetic form factors in the basis representation

In the basis representation, Eq. (25) becomes

$$\begin{aligned} & I_{m',m_J}(Q^2) \\ & = \sum_{n'm'l'} \sum_{nml} \sum_{rs} \psi_{n'm'l'rs}^* \psi_{nm lrs} \\ & \times \int \frac{dx}{4\pi x(1-x)} \chi_{l'}(x) \chi_l(x) \int \frac{d\vec{k}}{(2\pi)^2} \\ & \times \left\{ e_q \phi_{n'm'}^* \left(\frac{\vec{k}^{\perp} + (1-x)\vec{q}^{\perp}}{\sqrt{x(1-x)}} \right) \right. \\ & \quad \left. - e_{\bar{q}} \phi_{n'm'}^* \left(\frac{\vec{k}^{\perp} - x\vec{q}^{\perp}}{\sqrt{x(1-x)}} \right) \right\} \phi_{nm} \left(x, \vec{k}^{\perp} \right) \\ & = \sum_{n'm'l'} \sum_{nml} \sum_{rs} \psi_{n'm'l'rs}^* \psi_{nm lrs} \\ & \times \int \frac{dx}{4\pi x(1-x)} \chi_{l'}(x) \chi_l(x) \int \frac{d\vec{k}}{(2\pi)^2} \quad (\text{C14}) \\ & \times \left\{ e_q \phi_{n',-m'} \left(\frac{\vec{k}^{\perp} + (1-x)\vec{q}^{\perp}/2}{\sqrt{x(1-x)}} \right) \right. \\ & \quad \times \phi_{nm} \left(\frac{\vec{k}^{\perp} - (1-x)\vec{q}^{\perp}/2}{\sqrt{x(1-x)}} \right) \\ & \quad \left. - e_{\bar{q}} \phi_{n',-m'} \left(\frac{\vec{k}^{\perp} - x\vec{q}^{\perp}/2}{\sqrt{x(1-x)}} \right) \right. \\ & \quad \left. \times \phi_{nm} \left(\frac{\vec{k}^{\perp} + x\vec{q}^{\perp}/2}{\sqrt{x(1-x)}} \right) \right\}, \end{aligned}$$

where we have applied shifts in the transverse momentum and $\phi_{nm}^* = \phi_{n,-m}$.

We then apply the Talmi-Moshinsky (TM) transform to simplify the integrals in the transverse momentum [65, 76]. Specifically, the we have

$$\begin{aligned} & \phi_{n',-m'}(\vec{q}_1) \phi_{n,m}(\vec{q}_2) \\ & = \sum_{NM\bar{n}\bar{m}} C(n', -m', n, m; N, M, \bar{n}, \bar{m}) \\ & \quad \times \phi_{NM}(\vec{P}) \phi_{\bar{n}\bar{m}}(\vec{p}), \quad (\text{C15}) \end{aligned}$$

with all 4 harmonic oscillator functions sharing the same scale b and

$$\begin{cases} \vec{P} = (\vec{q}_1 + \vec{q}_2)/\sqrt{2} \\ \vec{p} = (\vec{q}_1 - \vec{q}_2)/\sqrt{2} \end{cases}, \quad (\text{C16})$$

which corresponds to

$$\begin{cases} \vec{P} = \frac{\sqrt{2}\vec{k}^\perp}{\sqrt{x(1-x)}} \\ \vec{p} = \sqrt{\frac{1-x}{2x}}\vec{q}^\perp \end{cases} \quad (\text{C17})$$

for the quark contribution and

$$\begin{cases} \vec{P} = \frac{\sqrt{2}\vec{k}^\perp}{\sqrt{x(1-x)}} \\ \vec{p} = -\sqrt{\frac{x}{2(1-x)}}\vec{q}^\perp \end{cases} \quad (\text{C18})$$

for the anti-quark contribution.

The coefficient $C(n', -m', n, m; N, M, \bar{n}, \bar{m})$ can be computed with established procedures [65, 76]. The following observations made specifically for the valence Fock sector of mesons will be helpful in enumerating terms after in the TM transform.

- Because the TM transform cannot change the total magnetic projection of the orbital angular momentum, we must have $-m' + m = M + \bar{m}$.
- The integral in \vec{k}^\perp will select the terms with $\bar{m} = 0$, leaving other values of m not contributing to the integral.
- Because the mesons obtained from the light-front Hamiltonian have fixed magnetic projection for the sum of the spin and orbital angular momenta, when the spins of the two wavefunction in a bilinear are identical, so are their magnetic quantum numbers m' and m .

These observations further confine us to $\bar{m} = -m' + m = 0$, which is expected since the electromagnetic form factors have no angular dependence.

The integrals over the momenta of the light-front wave functions then become

$$\begin{aligned} & \tilde{C}(n', m', l'; n, m, l; Q^2) \\ & \equiv \int \frac{dx}{4\pi x(1-x)} \chi_{l'}(x) \chi_l(x) \int \frac{d\vec{k}^\perp}{(2\pi)^2} \\ & \times \left\{ e_q \phi_{n', -m'} \left(\frac{\vec{k}^\perp + (1-x)\vec{q}^\perp/2}{\sqrt{x(1-x)}} \right) \right. \\ & \quad \left. \times \phi_{nm} \left(\frac{\vec{k}^\perp - (1-x)\vec{q}^\perp/2}{\sqrt{x(1-x)}} \right) \right. \end{aligned}$$

$$\begin{aligned} & - e_{\bar{q}} \phi_{n', -m'} \left(\frac{\vec{k}^\perp - x\vec{q}^\perp/2}{\sqrt{x(1-x)}} \right) \\ & \quad \left. \times \phi_{nm} \left(\frac{\vec{k}^\perp + x\vec{q}^\perp/2}{\sqrt{x(1-x)}} \right) \right\} \\ & = \int \frac{dx}{4\pi x(1-x)} \chi_{l'}(x) \chi_l(x) \\ & \quad \times \sum_{NM\bar{n}\bar{m}} C(n', -m', n, m; N, M, \bar{n}, \bar{m}) \int \frac{d\vec{k}^\perp}{(2\pi)^2} \\ & \quad \times \phi_{NM} \left(\frac{\sqrt{2}\vec{k}^\perp}{\sqrt{x(1-x)}} \right) \left\{ e_q \phi_{\bar{n}\bar{m}} \left(\sqrt{\frac{1-x}{2x}}\vec{q}^\perp \right) \right. \\ & \quad \left. - e_{\bar{q}} \phi_{\bar{n}\bar{m}} \left(-\sqrt{\frac{x}{2(1-x)}}\vec{q}^\perp \right) \right\} \\ & = \int \frac{dx}{4\pi} \chi_{l'}(x) \chi_l(x) \sum_{NM\bar{n}\bar{m}} \frac{(-1)^{N\bar{b}}}{2\sqrt{\pi}} \delta_{M0} \\ & \quad \times C(n', -m', n, m; N, M, \bar{n}, \bar{m}) \\ & \quad \times \left\{ e_q \phi_{\bar{n}\bar{m}} \left(\sqrt{\frac{1-x}{2x}}\vec{q}^\perp \right) \right. \\ & \quad \left. - e_{\bar{q}} \phi_{\bar{n}\bar{m}} \left(-\sqrt{\frac{x}{2(1-x)}}\vec{q}^\perp \right) \right\} \\ & = \delta_{m'm} \sum_{N\bar{n}} C(n', -m', n, m; N, 0, \bar{n}, 0) \\ & \quad \times \int \frac{dx}{4\pi} \chi_{l'}(x) \chi_l(x) \frac{(-1)^{N\bar{b}}}{2\sqrt{\pi}} \\ & \quad \times \left\{ e_q \phi_{\bar{n}0} \left(\sqrt{\frac{1-x}{2x}}\vec{q}^\perp \right) \right. \\ & \quad \left. - e_{\bar{q}} \phi_{\bar{n}0} \left(-\sqrt{\frac{x}{2(1-x)}}\vec{q}^\perp \right) \right\} \\ & = \delta_{m'm} \sum_{N\bar{n}} C(n', -m', n, m; N, 0, \bar{n}, 0) \\ & \quad \times \int \frac{dx}{4\pi} \chi_{l'}(x) \chi_l(x) (-1)^N \\ & \quad \times \left\{ e_q \exp \left(-\frac{1-x}{2x} \frac{Q^2}{2b^2} \right) L_{\bar{n}} \left(\frac{1-x}{2x} \frac{Q^2}{b^2} \right) \right. \\ & \quad \left. - e_{\bar{q}} \exp \left(-\frac{x}{2(1-x)} \frac{Q^2}{2b^2} \right) L_{\bar{n}} \left(\frac{x}{2(1-x)} \frac{Q^2}{b^2} \right) \right\}. \quad (\text{C19}) \end{aligned}$$

With the aid of the TM transform, the electromagnetic form factors in the basis representation be-

comes

$$I_{m'_j, m_j}(Q^2) = \sum_{n'm'l'} \sum_{n, m, l} \sum_{r, s} \psi_{n'm'l'rs}^* \quad (C20)$$

$$\times \tilde{C}(n', m', l'; n, m, l; Q^2) \psi_{nm lrs} .$$

Appendix D: Multi-qubit observables for the $J_z = 0$ sector of the $N_{\max} = L_{\max} = 0$, $M_{\max} = 2$ Hamiltonian

Below we provide the multi-qubit expressions for observables discussed in Sec. III for the $J_z = 0$ sector of the BLFQ pion Hamiltonian.

The decay constant can be obtained from eq. (16) as

$$f_\pi = 61.6 |\langle v | \psi(\vec{\theta}) \rangle| , \quad (D1)$$

$$|v\rangle = (0, 1/\sqrt{2}, -1/\sqrt{2}, 0) .$$

In order to reduce the gate count, rather than using the circuit from Fig. 2, we expand the projector onto the $|v\rangle$ state in terms of Pauli operators:

$$|v\rangle\langle v| = \frac{1}{2} \begin{pmatrix} 0 & 0 & 0 & 0 \\ 0 & 1 & -1 & 0 \\ 0 & -1 & 1 & 0 \\ 0 & 0 & 0 & 0 \end{pmatrix} , \quad (D2)$$

$$|v\rangle\langle v|_{\text{direct}} = 0.5IIII - 0.25(IXXI + IYYI + IZII + IIZI) , \quad (D3)$$

$$|v\rangle\langle v|_{\text{compact}} = 0.25(II - XX - YY - ZZ) . \quad (D4)$$

and calculate the decay constant using $|\langle v | \psi(\vec{\theta}) \rangle| = \sqrt{\langle \psi(\vec{\theta}) | (|v\rangle\langle v|) | \psi(\vec{\theta}) \rangle}$.

The mass radius matrix is given by eq. (22), which when expressed in terms of qubit operators is:

$$\frac{3}{2b^2} I_m = \begin{pmatrix} 2.27 & 0 & 0 & 0 \\ 0 & 1.13 & 0 & 0 \\ 0 & 0 & 1.13 & 0 \\ 0 & 0 & 0 & 2.27 \end{pmatrix} , \quad (D5)$$

$$\frac{3}{2b^2} I_{m, \text{direct}} = -1.30(IIIZ + ZIII) - 0.65(IIZI + IZII) + 3.92IIII , \quad (D6)$$

$$\frac{3}{2b^2} I_{m, \text{compact}} = 1.96II + 0.65ZZ . \quad (D7)$$

The $\rho_{l=0, l'=0}$ density matrix of the parton distribution function is given by eqs. (23)-(24b), which when expressed in terms of qubit operators is:

$$\rho = \begin{pmatrix} 1 & 0 & 0 & 0 \\ 0 & 1 & 0 & 0 \\ 0 & 0 & 1 & 0 \\ 0 & 0 & 0 & 1 \end{pmatrix} , \quad (D8)$$

$$\rho_{\text{direct}} = 2IIII - 0.5(ZIII + IZII + IIZI + IIIZ) , \quad (D9)$$

$$\rho_{\text{compact}} = II . \quad (D10)$$

We calculate the elastic form factor matrix $F_P(Q^2)$, eq. (27), by discretizing Q^2 on the interval $0 \leq Q^2 \leq 5152900$, evaluating the matrix $\tilde{C}(n', m', l'; n, m, l; Q^2)$ for each value of Q^2 , and expanding it in terms of Pauli operators. For the sake of brevity, we do not include these explicit expressions for each point.

Appendix E: Bravyi-Kitaev encoding

Both Jordan-Wigner and Bravyi-Kitaev encoding allow one to store the second-quantized fermionic states in a quantum computer. Within the Jordan-Wigner encoding, each qubit stores the occupancy of a particular orbital [56]. Within the Bravyi-Kitaev encoding, the information about parity is distributed equally between the operators and states [57]. In practice, one typically uses the more efficient BK encoding. While a single fermionic orbital in BK encoding is represented by up to $O(\log N)$ qubits (instead of $O(N)$ in JW), the creation and annihilation operators are represented now by $\log N$ -local multi-qubit operators [57].

The BK-encoded basis states $|\dots b_2 b_1 b_0\rangle$ can be obtained from the JW-encoded states by means of the linear transformation $b_i = \sum_{ij} \mathcal{P}_{ij} f_j$ [59], where the entries of \mathcal{P}_{ij} are $\{0, 1\}$, and multiplication modulo 2 is implied. Such a transformation of states can be implemented efficiently on a quantum computer. Since the matrix \mathcal{P}_{ij} is lower-triangular [59], multiplication modulo 2 can be performed on qubits using the CNOT gates, starting from the *bottom* row. For example, in the case of four qubits, the encoded matrix has the form of

$$\mathcal{P}_{ij} = \begin{pmatrix} 1 & 0 & 0 & 0 \\ 1 & 1 & 0 & 0 \\ 0 & 0 & 1 & 0 \\ 1 & 1 & 1 & 1 \end{pmatrix} . \quad (E1)$$

The corresponding circuit is shown on Fig. 8.

In order to perform the simulation in the BK encoding, one adjusts the procedure outlined in Sec. IV A as follows: a) After preparing the JW-encoded initial state $|\psi_0\rangle$, one appends to the circuit a block converting JW-encoded states to BK-encoded ones as on Fig. 8; b) Eq. (34) is replaced with its BK version which changes the coefficients α_j in (35) and h_i in eq. (37).

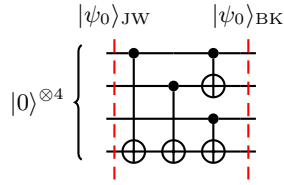


Figure 8. Converting a four-qubit state from Jordan-Wigner to Bravyi-Kitaev encoding.

-
- [1] Richard P. Feynman. Simulating physics with computers. *Int. J. Theor. Phys.*, 21(6):467–488, 1982.
- [2] Seth Lloyd. Universal quantum simulators. *Science*, 273(5278):1073–1078, 1996.
- [3] Christof Zalka. Simulating quantum systems on a quantum computer. *Proc. R. Soc. Lond. A*, 454(1969):313–322, 1998.
- [4] Stephen Wiesner. Simulations of many-body quantum systems by a quantum computer. 1996.
- [5] Bruce M Boghosian and Washington Taylor. Quantum lattice-gas models for the many-body schrödinger equation. *Int. J. Mod. Phys. C*, 8(04):705–716, 1997.
- [6] David A Meyer. From quantum cellular automata to quantum lattice gases. *J. Stat. Phys.*, 85(5-6):551–574, 1996.
- [7] Alán Aspuru-Guzik, Anthony D Dutoi, Peter J Love, and Martin Head-Gordon. Simulated quantum computation of molecular energies. *Science*, 309(5741):1704–1707, 2005.
- [8] L-A Wu, MS Byrd, and DA Lidar. Polynomial-time simulation of pairing models on a quantum computer. *Phys. Rev. Lett.*, 89(5):057904, 2002.
- [9] Stephen P. Jordan, Keith S. M. Lee, and John Preskill. Quantum algorithms for quantum field theories. *Science*, 336(6085):1130–1133, 2012.
- [10] Stephen P. Jordan, Keith S. M. Lee, and John Preskill. Quantum algorithms for fermionic quantum field theories. 2014.
- [11] Jonathan Olson, Yudong Cao, Jonathan Romero, Peter Johnson, Pierre-Luc Dallaire-Demers, Nicolas Sawaya, Prineha Narang, Ian Kivlichan, Michael Wasielewski, and Alán Aspuru-Guzik. Quantum information and computation for chemistry. 2017.
- [12] Joel E. Moore, Alán Aspuru-Guzik, Bela Bauer, Sue Coppersmith, Wibe de Jong, Thomas Devereaux, Marivi Fernandez-Serra, Giulia Galli, Robert Harrison, Thomas Maier, Antonio Mezzacapo, Jarrod McClean, Chris Monroe, John Preskill, Gus Scuseria, Birgitta Whaley, James Whitfield, Norman Yao, Dominika Zgid, Bruce Garrett, Jim Davenport, George Maracas, Linda Horton, Matthias Graf, Tom Russell, Jim Murphy, Jeff Krause, and Ceren Susut-Bennett. Opportunities for quantum computing in chemical and materials sciences. *DOE Basic Energy Sciences Roundtable Report*, 2017.
- [13] Alán Aspuru-Guzik, Wim Van Dam, Edward Farhi, Frank Gaitan, Travis Humble, Stephen Jordan, Andrew J Landahl, Peter J. Love, Robert Lucas, John Preskill, Richard P. Muller, Krysta Svore, Nathan Wiebe, and Carl Williams. Ascr workshop on quantum computing for science. Technical report, United States, 2015.
- [14] Dominic W Berry, Andrew M Childs, Richard Cleve, Robin Kothari, and Rolando D Somma. Exponential improvement in precision for simulating sparse hamiltonians. *Proceedings of the 46th Annual Symposium on Theory of Computing*, pages 283–292, 2014.
- [15] Guang Hao Low and Isaac L. Chuang. Optimal hamiltonian simulation by quantum signal processing. *Phys. Rev. Lett.*, 118:010501, 1 2017.
- [16] Guang Hao Low and Isaac L. Chuang. Hamiltonian Simulation by Qubitization. *Quantum*, 3:163, July 2019.
- [17] Dominic W Berry, Andrew M Childs, and Robin Kothari. Hamiltonian simulation with nearly optimal dependence on all parameters. In *2015 IEEE 56th Annual Symposium on Foundations of Computer Science*, pages 792–809. IEEE, 2015.
- [18] Dominic W Berry, Andrew M Childs, Richard Cleve, Robin Kothari, and Rolando D Somma. Simulating hamiltonian dynamics with a truncated taylor series. *Phys. Rev. Lett.*, 114(9):090502, 2015.
- [19] Uwe-Jens Wiese. Towards quantum simulating qcd. *Nucl. Phys. A*, 931:246–256, 2014.
- [20] Erez Zohar, J Ignacio Cirac, and Benni Reznik. Quantum simulations of lattice gauge theories using ultracold atoms in optical lattices. *Rep. Prog. Phys.*, 79(1):014401, 2015.
- [21] Erez Zohar, J Ignacio Cirac, and Benni Reznik. Cold-atom quantum simulator for su(2) yang-mills lattice gauge theory. *Phys. Rev. Lett.*, 110(12):125304, 2013.
- [22] Erez Zohar, J Ignacio Cirac, and Benni Reznik. Quantum simulations of gauge theories with ultracold atoms: Local gauge invariance from angular-momentum conservation. *Phys. Rev. A*,

- 88(2):023617, 2013.
- [23] Daniel González-Cuadra, Erez Zohar, and J Ignacio Cirac. Quantum simulation of the abelian-higgs lattice gauge theory with ultracold atoms. *New J. Phys.*, 19(6):063038, 2017.
- [24] Xiang Zhang, Kuan Zhang, Yangchao Shen, Shuain-ing Zhang, Jing-Ning Zhang, Man-Hong Yung, Jorge Casanova, Julen S. Pedernales, Lucas Lamata, Enrique Solano, and Kihwan Kim. Experimental quantum simulation of fermion-antifermion scattering via boson exchange in a trapped ion. *Nat. Commun.*, 9(1):195, 2018.
- [25] Ian C. Cloët, Matthew R. Dietrich, John Arrington, Alexei Bazavov, Michael Bishof, Adam Freese, Alexey V. Gorshkov, Anna Grassellino, Kawtar Hafidi, Zubin Jacob, Michael McGuigan, Yannick Meurice, Zein-Eddine Meziani, Peter Mueller, Christine Muschik, James Osborn, Matthew Otten, Peter Petreczky, Tomas Polakovic, Alan Poon, Raphael Pooser, Alessandro Roggero, Mark Saffman, Brent VanDevender, Jiehang Zhang, and Erez Zohar. Opportunities for nucl. phys. & quantum information science. 2019.
- [26] Sean Barrett, Klemens Hammerer, Sarah Harrison, Tracy E Northup, and Tobias J Osborne. Simulating quantum fields with cavity qed. *Phys. Rev. Lett.*, 110(9):090501, 2013.
- [27] Kevin Marshall, Raphael Pooser, George Siopsis, and Christian Weedbrook. Quantum simulation of quantum field theory using continuous variables. *Phys. Rev. A*, 92(6):063825, 2015.
- [28] Ali Hamed Moosavian and Stephen Jordan. Faster quantum algorithm to simulate fermionic quantum field theory. *Phys. Rev. A*, 98:012332, 6 2018.
- [29] Christian W. Bauer, Wibe A. De Jong, Benjamin Nachman, and Davide Provasoli. A quantum algorithm for high energy physics simulations. 2019.
- [30] Esteban A Martinez, Christine A Muschik, Philipp Schindler, Daniel Nigg, Alexander Erhard, Markus Heyl, Philipp Hauke, Marcello Dalmonte, Thomas Monz, Peter Zoller, et al. Real-time dynamics of lattice gauge theories with a few-qubit quantum computer. *Nature*, 534(7608):516–519, 2016.
- [31] Christine Muschik, Markus Heyl, Esteban Martinez, Thomas Monz, Philipp Schindler, Berit Vogell, Marcello Dalmonte, Philipp Hauke, Rainer Blatt, and Peter Zoller. U (1) wilson lattice gauge theories in digital quantum simulators. *New J. Phys.*, 19(10):103020, 2017.
- [32] Junyu Liu and Yuan Xin. Quantum simulation of quantum field theories as quantum chemistry. 4 2020.
- [33] M. Kreshchuk, William M. Kirby, Gary Goldstein, Hugo Beauchemin, and Peter J. Love. Quantum Simulation of Quantum Field Theory in the Light-Front Formulation. 2020.
- [34] J. P. Vary, H. Honkanen, Jun Li, P. Maris, S. J. Brodsky, A. Harindranath, G. F. de Teramond, P. Sternberg, E. G. Ng, and C. Yang. Hamiltonian light-front field theory in a basis function approach. *Phys. Rev. C*, 81:035205, 3 2010.
- [35] Xingbo Zhao. Advances in Basis Light-front Quantization. *Few Body Syst.*, 56(6-9):257–265, 2015.
- [36] Yang Li, Pieter Maris, Xingbo Zhao, and James P. Vary. Heavy quarkonium in a holographic basis. *Physics Letters B*, 758(Supplement C):118 – 124, 2016.
- [37] Yang Li, Pieter Maris, and James P. Vary. Quarkonium as a relativistic bound state on the light front. *Phys. Rev.*, D96(1):016022, 2017.
- [38] Shuo Tang, Yang Li, Pieter Maris, and James P. Vary. B_c mesons and their properties on the light front. *Phys. Rev. D*, 98(11):114038, 2018.
- [39] Shuo Tang, Yang Li, Pieter Maris, and James P. Vary. Heavy-light mesons on the light front. *Eur. Phys. J. C*, 80(6):522, 2020.
- [40] Jiangshan Lan, Chandan Mondal, Shaoyang Jia, Xingbo Zhao, and James P. Vary. Parton Distribution Functions from a Light Front Hamiltonian and QCD Evolution for Light Mesons. *Phys. Rev. Lett.*, 122(17):172001, 2019.
- [41] Jiangshan Lan, Chandan Mondal, Meijian Li, Yang Li, Shuo Tang, Xingbo Zhao, and James P. Vary. Parton Distribution Functions of Heavy Mesons on the Light Front. *Phys. Rev. D*, 102(1):014020, 2020.
- [42] Jiangshan Lan, Chandan Mondal, Shaoyang Jia, Xingbo Zhao, and James P. Vary. Pion and kaon parton distribution functions from basis light front quantization and QCD evolution. *Phys. Rev. D*, 101(3):034024, 2020.
- [43] Shaoyang Jia and James P. Vary. Basis light front quantization for the charged light mesons with color singlet nambu-jona-lasinio interactions. *Phys. Rev. C*, 99:035206, 3 2019.
- [44] S. P. Klevansky. The Nambu-Jona-Lasinio model of quantum chromodynamics. *Rev. Mod. Phys.*, 64:649–708, 1992.
- [45] Stanley J. Brodsky, Hans-Christian Pauli, and Stephen S. Pinsky. Quantum chromodynamics and other field theories on the light cone. *Phys. Rept.*, 301:299–486, 1998.
- [46] James P. Vary et al. Trends and Progress in Nuclear and Hadron Physics: a straight or winding road. *Few Body Syst.*, 58(2):56, 2017.
- [47] U. Vogl, Matthias F. M. Lutz, S. Klimt, and W. Weise. Generalized SU(3) Nambu-Jona-Lasinio Model. Part 2. From Current to Constituent Quarks. *Nucl. Phys.*, A516:469–495, 1990.
- [48] U. Vogl and W. Weise. The Nambu and Jona Lasinio model: Its implications for hadrons and nuclei. *Prog. Part. Nucl. Phys.*, 27:195–272, 1991.
- [49] S. Klimt, Matthias F. M. Lutz, U. Vogl, and W. Weise. Generalized SU(3) Nambu-Jona-Lasinio Model. Part 1. Mesonic Modes. *Nucl. Phys.*, A516:429–468, 1990.
- [50] Sidney D. Drell and Tung-Mow Yan. Connection of elastic electromagnetic nucleon form factors at large Q^2 and deep inelastic structure functions near

- threshold. *Phys. Rev. Lett.*, 24:181–186, 1 1970.
- [51] Geoffrey B. West. Phenomenological model for the electromagnetic structure of the proton. *Phys. Rev. Lett.*, 24:1206–1209, 1970.
- [52] Stephen P. Jordan, Keith S. M. Lee, and John Preskill. Quantum computation of scattering in scalar quantum field theories. *Quantum Inf. Comput.*, 14(11-12):1014–1080, 2014.
- [53] Alberto Peruzzo, Jarrod McClean, Peter Shadbolt, Man-Hong Yung, Xiao-Qi Zhou, Peter J Love, Alán Aspuru-Guzik, and Jeremy L O’Brien. A variational eigenvalue solver on a photonic quantum processor. *Nat. Commun.*, 5, 2014.
- [54] Jonathan Romero, Ryan Babbush, Jarrod R McClean, Cornelius Hempel, Peter J Love, and Alán Aspuru-Guzik. Strategies for quantum computing molecular energies using the unitary coupled cluster ansatz. *Quantum Science and Technology*, 4(1):014008, oct 2018.
- [55] Rolando Somma, Gerardo Ortiz, James E Gubernatis, Emanuel Knill, and Raymond Laflamme. Simulating physical phenomena by quantum networks. *Phys. Rev. A*, 65(4):042323, 2002.
- [56] P. Jordan and E. Wigner. Über das paulische äquivalenzverbot. *Z. Phys.*, 47(9):631–651, 9 1928.
- [57] Sergey B Bravyi and Alexei Yu Kitaev. Fermionic quantum computation. *Ann. Phys.*, 298(1):210–226, 2002.
- [58] Jacob T Seeley, Martin J Richard, and Peter J Love. The Bravyi-Kitaev transformation for quantum computation of electronic structure. *J. Chem. Phys.*, 137(22):224109, 2012.
- [59] Andrew Tranter, Sarah Sofia, Jake Seeley, Michael Kaicher, Jarrod McClean, Ryan Babbush, Peter V. Coveney, Florian Mintert, Frank Wilhelm, and Peter J. Love. The bravyi-kitaev transformation: Properties and applications. *Int. J. Quantum. Chem.*, 115(19):1431–1441, 2015.
- [60] Kanav Setia and James D. Whitfield. Bravyi-kitaev superfast simulation of electronic structure on a quantum computer. *J. Chem. Phys.*, 148(16):164104, 2018.
- [61] Ryan Babbush, Dominic W Berry, Ian D Kivlichan, Annie Y Wei, Peter J Love, and Alán Aspuru-Guzik. Exponentially more precise quantum simulation of fermions in second quantization. *New J. Phys.*, 18(3):033032, 2016.
- [62] Borzu Toloui and Peter J. Love. Quantum algorithms for quantum chemistry based on the sparsity of the ci-matrix. 2013.
- [63] Guang Hao Low and Isaac L. Chuang. Optimal hamiltonian simulation by quantum signal processing. *Phys. Rev. Lett.*, 118:010501, Jan 2017.
- [64] Guang Hao Low and Isaac L. Chuang. Hamiltonian Simulation by Qubitization. *Quantum*, 3:163, July 2019.
- [65] Paul Wiecki, Yang Li, Xingbo Zhao, Pieter Maris, and James P. Vary. Basis light-front quantization approach to positronium. *Phys. Rev. D*, 91:105009, May 2015.
- [66] Google AI Quantum and Collaborators. Hartree-fock on a superconducting qubit quantum computer. *Science*, 369(6507):1084–1089, 2020.
- [67] Dave Wecker, Matthew B Hastings, and Matthias Troyer. Progress towards practical quantum variational algorithms. *Phys. Rev. A*, 92(4):042303, 2015.
- [68] Jarrod R McClean, Jonathan Romero, Ryan Babbush, and Alán Aspuru-Guzik. The theory of variational hybrid quantum-classical algorithms. *New J. Phys.*, 18(2):023023, 2016.
- [69] Stanley J. Brodsky, Hans-Christian Pauli, and Stephen S. Pinsky. Quantum chromodynamics and other field theories on the light cone. *Phys. Rep.*, 301(4):299 – 486, 1998.
- [70] V. V. Shende, S. S. Bullock, and I. L. Markov. Synthesis of quantum-logic circuits. *IEEE Transactions on Computer-Aided Design of Integrated Circuits and Systems*, 25(6):1000–1010, 2006.
- [71] Diogo Cruz, Romain Fournier, Fabien Gremion, Alix Jeannerot, Kenichi Komagata, Tara Tomic, Jarla Thiesbrummel, Chun Lam Chan, Nicolas Macris, Marc-André Dupertuis, and Clément Javerzac-Galy. Efficient quantum algorithms for ghz and w states, and implementation on the ibm quantum computer. *Advanced Quantum Technologies*, 2(5-6):1900015, 2019.
- [72] R. H. Byrd, P. Lu, J. Nocedal, and C. Zhu. A limited memory algorithm for bound constrained optimization. *SIAM J. Sci. Comput.*, 16:1190–1208, 1995.
- [73] M. J. Powell. A direct search optimization method that models the objective and constraint functions by linear interpolation. *Advances in optimization and numerical analysis*, pages 51–67, 1994.
- [74] Stanley J. Brodsky and Guy F. de Teramond. Light-Front Holography and AdS/QCD Correspondence. *QCD Downunder II Auckland , New Zealand, January 17-19, 2008*, 2008.
- [75] M. Abramowitz and I.A. Stegun. *Handbook of Mathematical Functions: With Formulas, Graphs, and Mathematical Tables*. Applied mathematics series. Dover Publications, 1964.
- [76] L. Chaos-Cador and E. Ley-Koo. Common generating functions of complete harmonic oscillator wave functions and transformation brackets in d dimensions. *International Journal of Quantum Chemistry*, 97(4):844–853, 2004.